

## X-ray study of the liquid and solid phases of the alkali metals in $\text{KC}_{24}$ - and $\text{RbC}_{24}$ -intercalated graphite single crystals

F. Rousseaux\*

*Laboratoire de Cristallographie, Unité de Recherche Associée 810, Université d'Orléans, Boîte Postale 6759, 45067 Orleans CEDEX, France*

R. Moret

*Laboratoire de Physique des Solides, Unité de Recherche Associée 02, Université de Paris-Sud, Bâtiment 510, 91405 Orsay CEDEX, France*

D. Guerard and P. Lagrange

*Laboratoire de Chimie du Solide Minéral, Unité de Recherche Associée 158, Université de Nancy I, Boîte Postale 239, 54506 Vandoeuvre les Nancy, France*

(Received 11 August 1989; revised manuscript received 15 December 1989)

We report a detailed x-ray scattering study of the structure of stage-2 K- and Rb-intercalated graphite single crystals, as a function of temperature. The graphite-host samples were characterized by a low level of stage impurities but the degree of stacking disorder was high. The diffuse scattering from the room-temperature two-dimensional (2D) liquidlike structure of the alkali metals has been measured. It reveals subtle but meaningful differences between K and Rb. The in-plane liquid-solid transitions and the associated growth of interlayer correlations (2D-3D crossover) have been studied through scans of the main and satellite reflections. The stacking faults of the graphite host appear to be transferred to the intercalate. In the case of  $\text{KC}_{24}$ , a model calculation based on an average hexagonal K layer, with a subsequent partial relaxation of the K atoms in the graphite sites, provides a good fit to the observed reflection intensities. At lower temperatures, the K layers are confirmed to undergo a hexagonal-oblique symmetry-breaking transition at  $T_L \sim 95$  K, while the Rb layers stay hexagonal down to 10 K. Moreover, complex stacking sequences of the intercalate develop as the temperature is reduced, and in  $\text{RbC}_{24}$  one observes a clear loss of the stacking correlations. This is due presumably to a frustration of the K sublattice coming from interlayer and intralayer interactions.

### I. INTRODUCTION

In recent years structural studies of graphite intercalation compounds (GIC's) have focused on several aspects such as staging transitions and stage disorder, two-dimensional (2D) liquid state of the intercalant, modulated and domain structures, commensurate-incommensurate transitions, and intercalate interlayer orderings. A significant improvement in the understanding of these phenomena has been gained from both detailed diffraction studies (mainly with x rays) and theoretical models, as described in recent reviews.<sup>1-6</sup> Most of these works have been concerned with bromine,  $\text{SbCl}_5$ ,  $\text{FeCl}_3$ , and  $\text{HNO}_3$  for the acceptor-type intercalants and with the alkali metals (AM's) for the donors (not to mention several important results on ternary GIC's). In this respect, heavy-alkali-metal GIC's, with the stage  $n \geq 2$ , are important materials because of their relative simplicity and the opportunity they offer to investigate most of the above-mentioned 2D or quasi-2D phenomena.

The present work deals with stage-2 potassium and rubidium GIC's. It follows previous studies from the same groups which used single-crystal x-ray methods, especially high-resolution photographic techniques, to examine the evolution of the ordering of the AM atoms as a function of temperature, from room temperature to 10 K.<sup>7-9</sup>

From these results and those of numerous other groups our knowledge of the structural properties of stage-2 heavy-AM GIC's is quite advanced already, as summarized below.

(i) The stacking of the graphite layers can be described by the rhombohedral sequence  $A/AB/BC/C$ , where  $A, B, C$  refer to the graphite and a solidus refers to the AM.<sup>10</sup> The graphite bounding layers are thus symmetrically positioned across the AM layer.

(ii) At room temperature the AM atoms form a 2D liquid (no interlayer correlations) which is incommensurate with the in-plane spacings of the graphite sublattice. The scattering pattern exhibits unusual features. The central liquidlike ring or halo of diffuse scattering exhibits a marked anisotropy in the intensity distribution. This was first noted by Parry<sup>11</sup> and characterized in more detail by Rousseaux *et al.*<sup>7-9</sup> Intensity maxima are centered about the set of  $\langle 10.0 \rangle_G$  graphite directions for K (Ref. 7) and about the set of  $\langle 11.0 \rangle_G$  graphite directions for Rb (Ref. 8) and Cs.<sup>11</sup>

In addition, similar diffuse scattering halos are repeated about the six graphite  $\{10.0\}_G$  reflections. These are clear evidence of the modulation of the AM liquid by its graphite host. Such effects have been analyzed theoretically by Reiter and Moss,<sup>12</sup> who also showed that the modulation potential contributes to the intensity of the graphite  $(hk.l)_G$  reflections. This was used to extract the

Fourier components of this potential<sup>13</sup> from which molecular-dynamics calculations were performed in the case of RbC<sub>24</sub>.<sup>14</sup> Similar studies are being carried out for KC<sub>24</sub>.<sup>15</sup> The dynamical aspects of the 2D liquid state have been studied in great details by Kamitakahara and Zabel<sup>16</sup> using inelastic neutron scattering and by Zabel, Magerl and co-workers<sup>17</sup> using quasielastic neutron scattering. From these studies it appears that the liquid state is very peculiar in that both liquidlike diffusive motions and solidlike phonon excitations coexist over a broad temperature range. Accordingly the liquid-solid transition is continuous, and this behavior is attributed to the influence of the graphite-host potential.

(iii) Upon cooling the AM atoms order through liquid-solid transitions at temperatures  $T_c$  of 123.5, 156, and 165 K for K, Rb, and Cs, respectively. The characteristics of these transitions have been documented by a number of studies following the pioneering work of Nixon, Parry, and co-workers.<sup>10,11,18</sup> As the temperature is reduced from room temperature the intensity modulations of the diffuse scattering in the halos increase, and at  $T_c$  Bragg peaks emerge from the maxima. The transition is continuous and it is accompanied by a crossover from 2D to 3D correlations. Below  $T_c$  the ( $hkO$ ) diffraction patterns are composed of main reflections from a hexagonal lattice and satellite reflections produced by modulation from the graphite host.

The basic hexagonal lattice can be viewed as originating from a 2D close-packed arrangement of AM atoms, incommensurate with the graphite and rotated by  $\theta$  with respect to the graphite lattice. The primary unit vector  $q_{10,0}$  of the incommensurate lattice and its rotation angle  $\theta$  depend on the AM:

$$\text{K: } q_{10,0}^{\text{K}} = 1.26 \text{ \AA}^{-1}, \quad \theta = 7.5^\circ,$$

$$\text{Rb: } q_{10,0}^{\text{Rb}} = 1.225 \text{ \AA}^{-1}, \quad \theta = 11^\circ,$$

$$\text{Cs: } q_{10,0}^{\text{Cs}} = 1.158 \text{ \AA}^{-1}, \quad \theta = 14.5^\circ,$$

at low temperature. Below  $T_c$  there is practically no change in the values of  $q_{10,0}$  and  $\theta$  as  $T$  is decreased (although a weak temperature dependence was reported for Cs.<sup>19,20</sup> On the other hand, the main and satellite reflections grow continuously in intensity upon cooling.<sup>7,8,21,22</sup> In the case of K, Zabel *et al.*<sup>22</sup> attempted to derive a critical exponent  $\beta$  for the order parameter, according to a power law of the form  $I = A[(T_c - T)/T_c]^{2\beta}$  for the intensity, and they obtained  $\beta = 0.18 \pm 0.01$ , which is intermediate between predictions for 2D and 3D correlations. Actually the determination of the exponent in intercalated graphite samples [highly oriented pyrolytic graphite (HOPG) in this case] may be difficult because of the large number of faults and possible heterogeneities.

(iv) The structure of low-temperature ordered state and in particular the nature of the modulation have received a lot of attention. A structural model was first proposed by Clarke *et al.*,<sup>23</sup> who considered domains in which the AM atoms form a  $p(\sqrt{7} \times \sqrt{7})R$  19.11° superlattice (primitive triangular 2D lattice, commensurate and rotated by 19.11° relative to the graphite lattice). The degeneracy of this superlattice with respect to the graphite lat-

tice is 7, so that one has to consider seven equivalent domains assumed to be separated by a regular array of domain walls or discommensurations. This model was then extended by Yamada and Naiki,<sup>24</sup> Suzuki and Suematsu,<sup>25</sup> and Suzuki<sup>26</sup> using thermodynamical arguments analogous to those utilized for some charge-density-wave systems. From a free-energy minimization they could derive the characteristics of the discommensuration-domain structure (size of the domains, orientation and nature of the domain walls). These energy arguments also allow us to understand the origin of a universal relation between the incommensurability  $z = q_{10,0}/G_{10,0}$  [ $G_{10,0}$  is the (100) wave vector of graphite] and the rotation angle  $\theta$ , which is valid for the three stage-2 AM GIC's and was discovered by Mori *et al.*,<sup>27</sup>

$$\cos(30^\circ - \theta) = (1 + z^2)/(2 + \sqrt{3}z).$$

While the discommensuration-domain model appears to be satisfactory in the case of Cs (18–19 atoms per domain), it leads to domain sizes which are so small in the case of Rb (8–9 atoms) and especially of K (3–4 atoms) (Ref. 9) that the description of the atomic order in terms of distinct ( $\sqrt{7} \times \sqrt{7}$ ) domains is not appropriate any more. Moreover, the corresponding calculated intensities do not fit the observed values in the case of KC<sub>24</sub> and stage-3 CsC<sub>36</sub> very well.<sup>26</sup> In the latter case a significant improvement of the fit was obtained by allowing the atoms to relax, resulting in a net rotation of the domains about their centers.<sup>28</sup>

A different approach was chosen by Diczio,<sup>29</sup> who started from an incommensurate close-packed layer of AM atoms as defined by  $q_{10,0}$ , rotated it by  $\theta$  with respect to the graphite (maximizing the  $\theta$  value to favor  $\sqrt{7} a_G$  distances), and relaxed the AM atoms into the nearest hexagon centers. Although this procedure is not based on explicit thermodynamical grounds, it is able to provide a plausible description of the ordered state and leads to a rather good fit of the experimental and calculated intensity data, as will be shown later.

To illustrate the difficulty of evaluating the validity of these 2D structural models from a too limited set of intensity data, we mention the opposite hypothesis of Mori *et al.*,<sup>27</sup> who considered that the graphite lattice, not the AM one, was modulated. Surprisingly, they could obtain a rather good fit of the data, although the graphite distortions had to be taken unphysically large.

(v) In the case of RbC<sub>24</sub> and CsC<sub>24</sub> the effect of reducing the temperature well below  $T_c$  is only to increase the intensity of the high-order reflections, which indicates a strengthening of the modulation potential. In contrast, KC<sub>24</sub> exhibits a second transition at  $T_L = 95$  K with a dramatic change of the ( $hk.0$ ) diffraction pattern. Although it was suggested by Winokur and Clarke<sup>30</sup> that a fragmentation into high-order commensurate phases could account for the observed pattern, Rousseaux *et al.*<sup>8</sup> show that a better fit is obtained by using a simple incommensurate oblique lattice. This will be confirmed here, and it raises the interesting problem of the driving force of this hexagonal-oblique symmetry-breaking

phenomenon.

(vi) Finally we point out that the nature of the stacking correlations of the AM layers which has been given some attention, especially in the case of Rb and Cs, is still very unclear. It appears that an unusual loss of stacking coherence can occur upon cooling<sup>28,31</sup> and it was suggested that the competition between interlayer and intralayer forces could explain this effect.<sup>31</sup> Complementary results will be given here.

The purpose of the present study is to provide detailed quantitative structural data on the liquid and solid phases of  $\text{KC}_{24}$  and  $\text{RbC}_{24}$  single crystals. Particular attention is given to the modulation effect in the liquid state, the liquid-solid transition, and the temperature dependence of the intercalate-layer stacking correlations. Structural models for the ordered structures of  $\text{KC}_{24}$  are presented and tested through a comparison with the experimental data.

The paper is organized as follows. The experimental details are given in Sec. II. In Sec. III we deal with the characterization of the stage and of the graphite-layer stacking. In Sec. IV we provide detailed data about the liquid diffuse scattering. The characteristics of the liquid-solid transitions are described in Sec. V. In Sec. VI we present and discuss different structural models for the low-temperature phases of  $\text{KC}_{24}$ .

## II. EXPERIMENTAL PROCEDURE

### A. Sample preparation

Natural single-crystal graphite flakes of high quality and relatively large size (typically  $1.5 \times 6 \times 0.3 \text{ mm}^3$ ) were selected and used as host materials. Intercalation was achieved using the two-zone method in which the intercalant was maintained at a temperature  $T_i$  (393 K) and the graphite was held at a higher temperature  $T_g$  during 2 or 3 days. The difference  $T_g - T_i$  (120 K for K, 180 K for Rb) was chosen to obtain stage-2 compounds with the maximum in-plane concentration of alkali metal (between  $\text{MC}_{20}$  and  $\text{MC}_{22}$  where  $M$  represents the alkali metal). Nevertheless, according to common use we shall name these stage-2 AM compounds  $\text{KC}_{24}$  or  $\text{RbC}_{24}$  in the following. After reaction the samples were sealed off, under inert atmosphere, in a Lindeman glass tube.

Because of the high reactivity of the samples with regards to oxygen and water, it is crucial that no traces of these contaminants are present, which is difficult during the sealing procedure. A slight contamination may have occurred in the present case, which would be responsible for the presence of a small percentage of stage 3, in particular for the  $\text{KC}_{24}$  sample (see Sec. III A). This degradation is probably limited to regions of the crystal which are close to the surface. As shown later, we consider that the interpretation of our results is not hindered by this limited stage impurity.

### B. X-ray measurements

Diffraction measurements were performed with copper radiation ( $\text{Cu } K\alpha$ ,  $\lambda = 1.5418 \text{ \AA}$ ) using two

different diffractometers. Most of the data were collected with a two-axis diffractometer using a lifting-detector geometry. The x-ray beam from a rotating anode generator (60 kV, 150 mA) was focused by a doubly bent graphite monochromator and the scattered beam was measured with a scintillation detector. The sample was rotated about an in-plane graphite axis (noted  $b$ ) so that the  $a^*$  and  $c^*$  axes were horizontal. The measurements were made in transmission and the resolution  $\Delta q$  corresponding to the half width at half maximum (HWHM) was estimated to be  $0.02 \text{ \AA}^{-1}$ . A more limited set of data was obtained on a second instrument equipped with a linear position-sensitive detector.

For both data collections the Lindeman tubes containing the samples were attached with silver paste to the cold end of a helium close-cycle refrigerator and the temperature could be varied from 10 to 300 K with a stability of 0.3 K. Since the samples were suspended in the glass tubes and not in direct contact with the cold end, special attention was given to the thermalization. Two concentric thermal shields were installed and time was allowed for the sample temperature to equilibrate.

The scattering from the sample was corrected for the contribution of the Lindeman tube. This amorphous background was measured at room temperature and low temperature (130 and 12 K) without the graphite sample (by shifting the tube to remove the sample from the x-ray beam). The temperature dependence was found to be negligible. Figure 1 shows a  $(\theta - 2\theta)$  scan of this glass scattering in the horizontal plane of the diffractometer at  $T = 295 \text{ K}$ . It corresponds to the graphite  $\langle 10.0 \rangle_G$  direction. We also performed an angular scan at constant  $q$  value ( $q = 1.20 \text{ \AA}^{-1}$ ) to probe the glass scattering in the diffractometer setting used for measuring the AM scattering in the  $(hk0)_G$  plane. It showed no dependence of the glass scattering,  $I_{\text{glass}}$ , on the angle  $\varphi$  ( $\varphi$  is defined in Fig. 4).

The contribution of the glass tube was subtracted according to

$$I_{\text{graphite}} = I_{\text{measured}} - kI_{\text{glass}}$$

The value of the coefficient  $k$  ( $k < 1$ ) involves the absorption of the sample which reduces the magnitude of the glass scattering. We did not attempt to calculate  $k$ ,

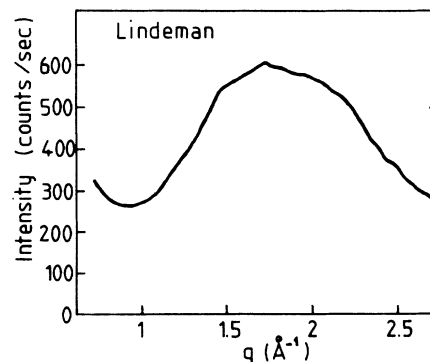


FIG. 1. Radial  $(\theta - 2\theta)$  scan along the graphite  $\text{G}_{10.0}$  direction of the x-ray diffuse scattering from the capillary tube. A broad amorphous peak is centered at about  $q = 1.8 \text{ \AA}^{-1}$ .

which was taken somewhat arbitrarily to be independent of the scattering vector. We estimated  $k=0.85$ , which provides reasonable values for the background intensity levels for all types of scans. The broad amorphous peak visible in the radial scan of Fig. 1 shows how important it is to subtract the glass contribution, especially for the liquid phase, because the liquid scattering is weak and displays important features in the same  $q$  range. An improvement of the correction would require an estimation, by measurement or calculation of the sample absorption, of the  $q$  dependence of  $k$ .

### III. STAGING AND STACKING

#### A. Staging

Figure 2 shows typical scans in the  $c^*$  direction ( $\theta-2\theta$  geometry) for stage determination at room temperature and 12 K for  $\text{KC}_{24}$ . Most of the peaks can be attributed to the stage-2 sequence and their  $l$  indexes are indicated. Note that for the  $(00.l)$  reflections (only for them) we define  $l$  with respect to the distance, in real space, between successive intercalate layers, noted  $I_c$ . These  $l$  values have to be multiplied by 3 when one considers the true repeat distance along  $c$ , i.e.,  $3I_c$ , originating from the rhombohedral stacking of the graphite layers (see subsection B).

The  $(00.l)$  reflections were scanned from  $l=4$  to 8 for  $\text{KC}_{24}$  (Fig. 2). Extra peaks (shaded) correspond to 15% stage-3 contamination at room temperature, as estimated from the ratios of the  $(00.5)$ -stage-2 to  $(00.7)$ -stage-3 reflections. In the case of  $\text{RbC}_{24}$  the amount of stage 3 was only 3% at room temperature.

When the temperature was lowered to 12 K no significant change could be observed in the case of  $\text{KC}_{24}$  and the amount of stage 3 remained the same. In contrast, an increase of the fraction of stage 3 was found for  $\text{RbC}_{24}$  upon cooling. Furthermore, a very small stage-4 contamination appeared. No attempt was made to characterize these transformations quantitatively, although we can assert that they involved less than 10% of the sample.

It is difficult to estimate the possible influence of these stage impurities and stage transformations on the ordering of the AM intercalant, which is our main concern here. The existence of the stage-3 contamination, especially in  $\text{KC}_{24}$ , does indicate that, contrary to what we expected from the preparation conditions, the AM content of our samples may have not been maximized. The temperature-induced stage transformation in  $\text{RbC}_{24}$  is also puzzling when compared to the few available reports of such effects. While Winokur and Clarke<sup>30</sup> report no change of stage in  $\text{KC}_{24}$ , a detailed investigation by Cajipe and Fischer<sup>32</sup> found a significant stage-2-stage-3 transformation (with phase separation) in stage-2 samples which were already partially mixed at room temperature. A stage-2-stage-3 transition at low  $T$  induces a densification of the AM layers (assuming no change in the global AM density, i.e., no loss of AM). In already dense and almost pure stage-2 samples this is certainly unfavorable, which agrees with the Cajipe and Fischer

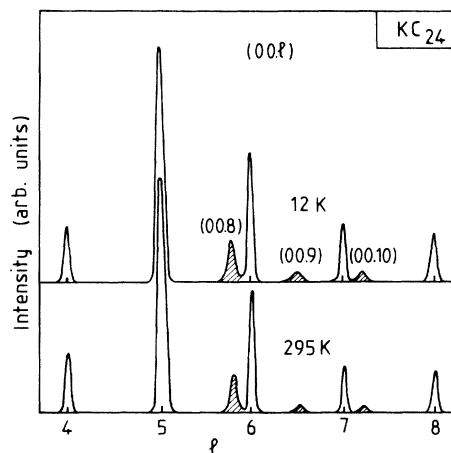


FIG. 2.  $(00.l)$  scans of a  $\text{KC}_{24}$  single crystal at room temperature and 12 K. The stage-2  $(00.l)$  peaks from  $l=4-8$  are displayed along with stage-3  $(00.8)$ ,  $(00.9)$ , and  $(00.10)$  impurity peaks. No significant change with temperature is detected.

findings. Our results are thus unexpected, since we observed a stage transformation in  $\text{RbC}_{24}$  only, although its second stage is purer than that of  $\text{KC}_{24}$  at room temperature.

Cajipe and Fischer also reported a dependence of the in-plane low- $T$  structure on stage mixing and stage transitions. It is certainly true that the in-plane density plays a significant role in the details of the in-plane AM ordering. However, we do not think that it is important enough to change the low- $T$  in-plane structure of  $\text{KC}_{24}$  as drastically as reported in Ref. 32, where a low- $T$  single phase is found at high AM density and a completely different multiple-phase structure for a slightly lower density. Moreover, our previous experience with single crystals of slightly different AM concentrations (due to uncontrolled sample preparation and transfer effects) indicates that the present 10–15% range of stage impurities should not alter the behavior of the AM ordering dramatically. This is certainly a reasonable statement when considering intralayer effects, while some interlayer ones may be influenced by these stage impurities.

#### B. Stacking of the graphite layers

The stacking of the graphite layers was investigated through scans along the graphite  $(10.l)$  and  $(20.l)$  reciprocal-lattice rows for both  $\text{KC}_{24}$  and  $\text{RbC}_{24}$  compounds. Figure 3 shows the  $(10.l)$  intensity profiles (dots) measured at room temperature and limited for technical reasons to  $l=9$  ( $\text{KC}_{24}$ ) and  $l=13$  ( $\text{RbC}_{24}$ ). In the case of a long-range ordered rhombohedral stacking sequence of the type  $A/AB/BC/C$ , as expected for a stage-2 alkali-metal GIC, one should observe sharp peaks for  $l \neq 3n$ , where the  $l=3n$  reflections are absent. Also strong reflections should be observed for  $l=4$  and 5. In contrast, the experimental profiles of Fig. 3 display no sharp peaks at integer  $l$  values but only broad maxima. This is due to the reflections being dramatically broadened and shifted because of the large amount of stacking faults in

the graphite sublattice. Moreover, the stage-3 regions give a significant contribution to the  $(10.l)$  profile in the case of  $\text{KC}_{24}$ .

The  $(10.l)$  experimental profiles have been analyzed and fitted with intensity distributions calculated by introducing a variable fraction of stacking faults with respect to the deal  $A/AB/BC/C$  stacking sequence. The model involves a basic unit formed by a sandwich graphite-alkali-metal-graphite (either  $A/A$ ,  $B/B$ , or  $C/C$ ) of thickness  $I_c$ , where  $I_c$  is the repeat distance along  $c$  given by the  $(00l)$  reflections. In the ideal stacking sequence there are three sandwiches related by a translation  $\Delta + \mathbf{I}_c$ , with  $\Delta = \frac{1}{3}\mathbf{a}_G + \frac{2}{3}\mathbf{b}_G$  and  $\mathbf{a}_G$ ,  $\mathbf{b}_G$  the in-plane unit vectors of graphite. It corresponds to a rhombohedral symmetry. A stacking fault occurs when two neighboring sandwiches are related by  $-\Delta + \mathbf{I}_c$ . The calculation involves nearest-neighbor interactions which can be expressed using a matricial formalism.

Two parameters are varied to fit the calculated profiles to the experimental ones:

- (i) the frequency of occurrence of a translation  $+\Delta$ :  $f_+$
- (ii) the conditional probability of having a sequence  $+\Delta, -\Delta$ :  $P_{+-}$  and these probabilities are constrained by relations such as  $f_+P_{+-} = f_-P_{-+}$ . In addition, to improve the fit it was necessary to introduce "nonhexago-

nal" stacking faults (no longer within the  $A, B, C$  scheme) with arbitrary translations between the graphite-AM-graphite sandwiches. The probability of such faults, distributed at random, is called  $P_r$ .

A further complication in the analysis of the  $(10.l)$  profiles comes from the contribution of the disordered AM atoms to the Bragg reflections of the graphite sublattice, as pointed out in the Introduction. A rigorous treatment of this effect can be performed using the formalism developed by Reiter and Moss<sup>12</sup> to obtain the Fourier components of the modulation potential. We did not attempt to carry out such an analysis, which requires a careful measurement of a set of graphite reflections, which was not our purpose. Therefore we have limited ourselves to try to obtain a reasonable fit to the experimental  $(10.l)$  profiles in order to estimate the degree of faulting and, for  $\text{KC}_{24}$ , the effects of the stage-3 contamination. Accordingly we have introduced in the fitting procedure a parameter  $X$  that represents somewhat arbitrarily the fraction of AM atoms which are registered, i.e., in graphite hexagon centers. Similar analyses were carried out previously by Rousseaux *et al.*<sup>33</sup> for  $\text{KC}_{24}$ ,  $\text{RbC}_{24}$ , and  $\text{CsC}_{24}$ , and by Ohshima *et al.*<sup>34</sup> for  $\text{RbC}_{24}$ .

The calculated profile for  $\text{KC}_{24}$  [Fig. 3(a)] was obtained with  $f_+ = 0.75$ ,  $P_{+-} = 0.25$ , and  $P_r = 0.20$  and a fraction of registered K atoms  $X = 57\%$  at room temperature. For  $\text{RbC}_{24}$  [Fig. 3(b)] the corresponding best-fit parameters are  $f_+ = 0.78$ ,  $P_{+-} = 0.22$ ,  $P_r = 0.20$ , and  $X = 40\%$ . They provide reasonable fits to the data except for the shaded peaks in  $\text{KC}_{24}$  which correspond to the stage-3 contamination. For  $\text{RbC}_{24}$  the 3% stage-3 impurity is too small to be visible in the  $(10.l)$  profiles given the fairly large stacking-fault effect as evidenced by the values of  $P_{+-}$  and  $P_r$ . The  $(10.l)$  intensity profiles were also measured at  $T = 12$  K and fitted. No appreciable temperature dependence was observed for the stacking-fault concentrations. On the other hand, the fraction  $X$  increases on cooling to 86% and 57% for  $\text{KC}_{24}$  and  $\text{RbC}_{24}$ , respectively. Although these figures have to be used with caution, for the reasons mentioned previously, they undoubtedly reflect the increased influence of the graphite-layer potential in centering the AM atoms at low temperature.

#### IV. LIQUID STATE

We now present quantitative data on the AM diffuse scattering in the 2D liquid state for  $\text{KC}_{24}$  and  $\text{RbC}_{24}$ . The general features of this diffuse scattering were introduced in Sec. I, and they are schematized geometrically in Fig. 4 with a central halo around the origin, its harmonic, and a set of six similar halos centered about the  $\{10.0\}_G$  reciprocal lattice points of the graphite host.

The 2D nature of the interactions is evidenced by the continuous diffuse scattering intensity measured on the central halo, at  $q_{hk} = 1.20 \text{ \AA}^{-1}$  and scanned along  $c^*$ , as shown in Fig. 5. The slow decrease of the intensity with  $l$  is due to the decay of the scattering factor with  $q = 2\pi(\sin\theta/\lambda)$ . The absence of any intensity modulation in the profile shows that the K and Rb layers are not correlated at room temperature. We point out inciden-

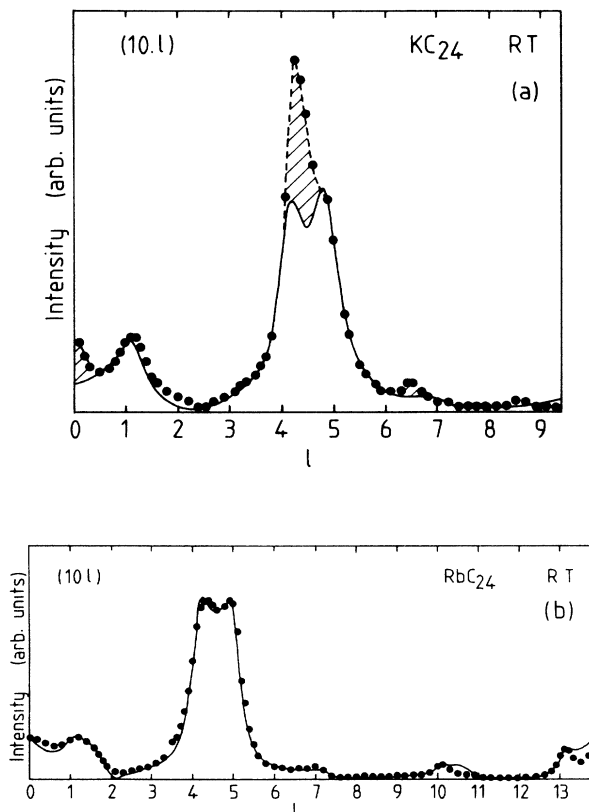


FIG. 3.  $(10.l)$  scans of  $\text{KC}_{24}$  (a) and  $\text{RbC}_{24}$  (b) at room temperature. The solid line is a fit to the data which takes account of stacking faults and of a contribution from the AM atoms. The hatched regions in (a) correspond to the stage-3 contribution in  $\text{KC}_{24}$ .

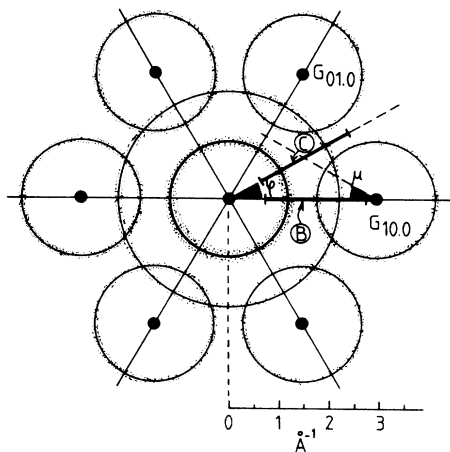


FIG. 4. Schematic representation of the  $(hk0)$  reciprocal lattice featuring the  $\{10.0\}_G$  graphite points (labeled  $G_{10.0}$  for instance in the figure) and the AM diffuse halos of the liquid state. Also indicated are the  $B$  and  $C$  scans described in Fig. 6 and the angle  $\varphi$  and  $\mu$  utilized to present the results of several scans. The scale in  $\text{\AA}^{-1}$  is also given at the bottom.

tally the larger intensity obtained in the case of  $\text{RbC}_{24}$  because of the stronger scattering power of  $\text{Rb}$  as compared with  $\text{K}$ . This behavior is general, and it made the experiment more difficult and less accurate in the case of  $\text{KC}_{24}$ .

Several types of scans were performed in the  $(hk.0)$  plane to study the 2D diffuse scattering distribution. Figure 6 shows radial intensity scans  $I(q)$  at  $\varphi=0^\circ$  and  $\varphi=30^\circ$  ( $\varphi$  is the azimuthal angle measured from  $G_{10.0}$ ) up to  $q \sim 2.6$ – $2.8 \text{ \AA}^{-1}$  for  $\text{KC}_{24}$  [part (a)] and  $\text{RbC}_{24}$  [(part (b))]. They correspond to scans  $B$  and  $C$  in Fig. 4. For  $\text{KC}_{24}$  one observes a main diffuse peak near  $q_1 = 1.2 \text{ \AA}^{-1}$  in scans  $B$  ( $\varphi=0^\circ$ ) and  $C$  ( $\varphi=30^\circ$ ). Moreover, secondary peaks are found at  $q_2 = 1.72 \pm 0.03 \text{ \AA}^{-1}$  and  $q_3 = 2.21 \pm 0.05 \text{ \AA}^{-1}$  for  $\varphi=0^\circ$  (scan  $B$ ). In the case of  $\varphi=30^\circ$  (scan  $C$ ) the data collection above  $2.3 \text{ \AA}^{-1}$  was not possible because of a blind region of the diffractometer. No peak at  $q_2$  is found and there is an increase of the intensity from  $q=2 \text{ \AA}^{-1}$  to  $q=2.25 \text{ \AA}^{-1}$  which is reminiscent of the  $q_3$  diffuse peak.

The three peaks at  $q_1$ ,  $q_2$ , and  $q_3$  can be easily attributed using in particular the previous photographic results<sup>7</sup>

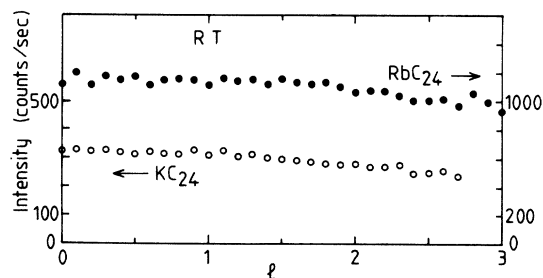


FIG. 5. Scan along  $l$  of the AM liquid scattering at  $q=1.20 \text{ \AA}^{-1}$  showing the 2D nature of the correlations in  $\text{KC}_{24}$  and  $\text{RbC}_{24}$  at room temperature.

and Fig. 4. The  $q_1$  peak corresponds to the central halo, the  $q_2$  peak arises from the halo centered about  $(10.0)_G$  and therefore it is not seen for  $\varphi=30^\circ$ , and the  $q_3$  peak comes from the harmonic of the central halo. The stronger intensity in the  $q_1$  peak for  $\varphi=0^\circ$ , as compared to  $\varphi=30^\circ$ , is in agreement with the existence of an intensity modulation in the central halo with maxima along  $\langle 10.0 \rangle_G$  as observed previously<sup>7</sup> in the case of  $\text{KC}_{24}$ .

Turning to the corresponding scans for  $\text{RbC}_{24}$  [Fig. 6(b)] one sees an opposite effect since the intensity at  $q_1$  is larger for  $\varphi=30^\circ$  than for  $\varphi=0^\circ$ . This is again a confirmation of a known feature, namely that maxima occur along  $\langle 11.0 \rangle_G$  in the case of  $\text{RbC}_{24}$  (Ref. 8) [as well as  $\text{CsC}_{24}$  (Ref. 11)]. Going to higher  $q$  values one observes a weak peak at  $q_2 = 1.75 \pm 0.05 \text{ \AA}^{-1}$  for  $\varphi=0^\circ$  (absent for  $\varphi=30^\circ$ ) which we attribute to the halo centered about  $(10.0)_G$ . Note that this peak is comparatively weaker than in  $\text{KC}_{24}$ . This is probably due again to the existence of intensity modulations in this secondary halo. Actually the scan at  $\varphi=0^\circ$  corresponds to an intensity minimum in the case of  $\text{RbC}_{24}$  and a maximum for  $\text{KC}_{24}$ .

For  $\text{RbC}_{24}$  above  $q=2 \text{ \AA}^{-1}$  the intensity varies smoothly with faint maxima at  $q \sim 2.25 \text{ \AA}^{-1}$  ( $\varphi=0^\circ$ ) and  $q \sim 2.5 \text{ \AA}^{-1}$  ( $\varphi=30^\circ$ ) and the contribution of the harmon-

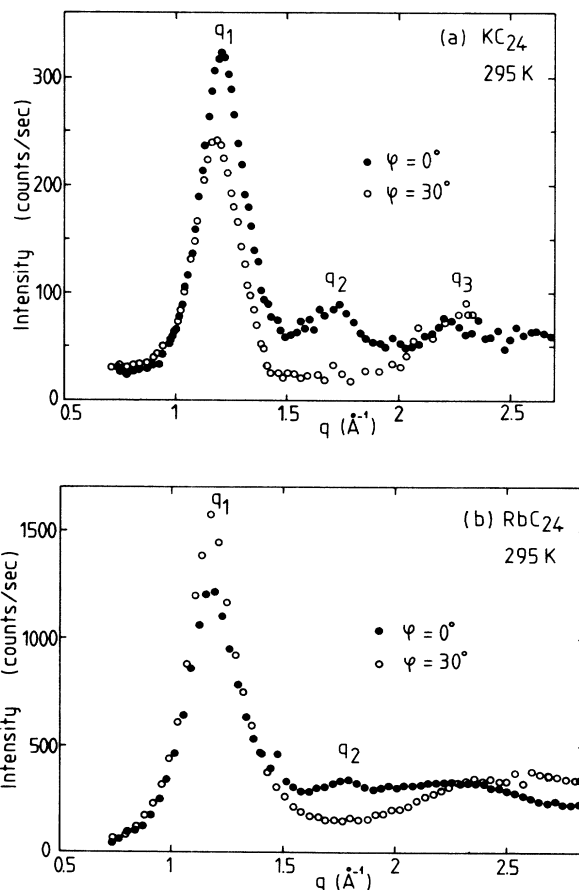


FIG. 6. Radial scans of the in-plane diffuse scattering at  $\varphi=0^\circ$  and  $30^\circ$  (scans  $B$  and  $C$  in Fig. 4) in  $\text{KC}_{24}$  (a) and  $\text{RbC}_{24}$  (b) at 295 K. The  $q_1$ ,  $q_2$ , and  $q_3$  peaks discussed in the text are indicated.

ic halo at  $q_3$  is not clear.

The profiles just described (Fig. 6) provide quantitative data that confirm the general features obtained with photographic x-ray methods.<sup>7,8</sup> In the following we describe more detailed scans which reveal new aspects of the modulated diffuse scattering. Figure 7 displays radial scans of the first halo at selected  $\varphi$  values between  $0^\circ$  and  $30^\circ$  for  $\text{KC}_{24}$  [part (a)] and  $\text{RbC}_{24}$  [part (b)]. The full  $(hk.l)$  plane could of course be reconstructed using the symmetry elements of the two-dimensional point-group  $6mm$ . For  $\text{KC}_{24}$  there is a clear shift of the peak towards lower  $q$  values going from  $q_1 = 1.215 \text{ \AA}^{-1}$  at  $\varphi = 0^\circ$  to  $q_1 = 1.190 \text{ \AA}^{-1}$  at  $\varphi = 30^\circ$ . This shift implies that the halo is not strictly circular and its geometry may be best described as intermediate between a circle and hexagon whose vertices point along  $\{10.0\}_G$ . Such an effect is only barely visible at 300 K in the stationary photograph of Ref. 7, but it becomes clearer at 200 K. It undoubtedly reflects the characteristics of the modulation potential from the graphite. In  $\text{RbC}_{24}$  this "hexagonality" of the central halo is also present, though weaker, and  $q_1$  decreases from  $q_1 = 1.195 \text{ \AA}^{-1}$  ( $\varphi = 0^\circ$ ) to  $q_1 = 1.18 \text{ \AA}^{-1}$  ( $\varphi = 30^\circ$ ). This feature is actually reproduced in the  $S(q)$  derived from the molecular-dynamics (MD) study of 2D Rb liquid in graphite as recently performed by Fan *et al.* (see Fig. 9). The reasons for the more pronounced hexagonality of the halo in the case of  $\text{KC}_{24}$  proceed from the details of the modulation potential. Comparing the values of its Fourier coefficients,  $\beta V_{HK}$ , and the associated contour maps determined by Moss and co-workers for

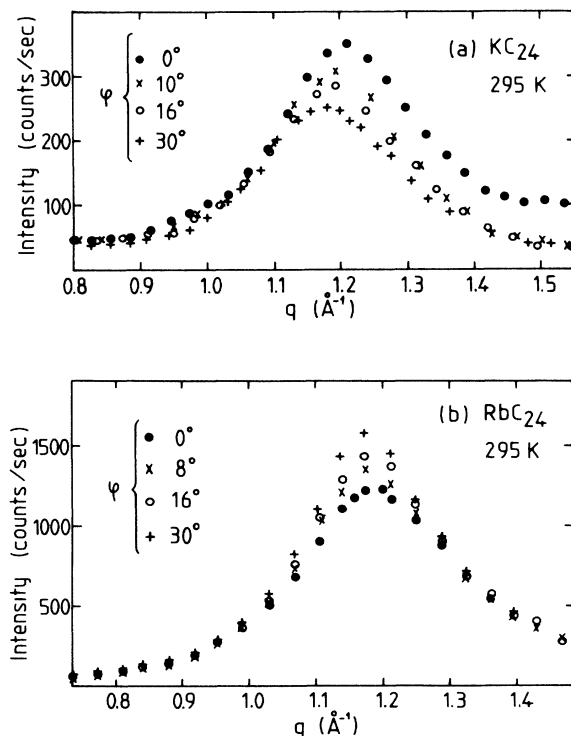


FIG. 7. Radial scans of the  $q_1$  peak in  $\text{KC}_{24}$  (a) and  $\text{RbC}_{24}$  (b) at room temperature. They reveal a significant shift of the peak position and the modulation of the intensity along the halo.

$\text{RbC}_{24}$  and  $\text{KC}_{24}$  (Refs. 13–15 and 35) it appears immediately that the "hexagonal character" of the potential is more prominent for  $\text{KC}_{24}$  because of significant Fourier coefficients at higher  $q$  and especially of a relatively large  $\beta V_{11}$  ( $-0.19$ ) which is almost half of  $\beta V_{10}$  ( $-0.41$ ).<sup>35</sup> In contrast, for  $\text{RbC}_{24}$ , the  $\beta V_{10}$  coefficient is the only strong one. It is therefore normal to observe a stronger hexagonal-like distortion of the halo in  $\text{KC}_{24}$  than in  $\text{RbC}_{24}$ .

The radial width of the halo can be measured from the scans of Fig. 7. It appears to increase slightly from  $\varphi = 0^\circ$  to  $\varphi = 30^\circ$  as the half width at half maximum,  $\Delta q_{1/2}$ , goes from  $0.11 \text{ \AA}^{-1}$  to about  $0.12 \text{ \AA}^{-1}$  for both  $\text{KC}_{24}$  and  $\text{RbC}_{24}$ . This yields correlation lengths  $\xi = 1/\Delta q_{1/2}$ , on the order of  $8\text{--}9 \text{ \AA}$  at room temperature.

The angular modulation of the diffuse scattering in the halos was further characterized through radial scans of the central and secondary halos as a function of the angles  $\varphi$  and  $\mu$  ( $\mu$  is defined in Fig. 4). Figure 8 is concerned with the central halo, and gives the maximum intensity obtained from the radial scans versus  $\varphi$ . The opposite behaviors of  $\text{KC}_{24}$  and  $\text{RbC}_{24}$  are clear, the intensity decreasing and increasing with  $\varphi$  for  $\text{KC}_{24}$  and  $\text{RbC}_{24}$ , respectively. Furthermore, weak and broad shoulders are observed, centered at roughly  $\varphi = 8^\circ$  ( $\text{KC}_{24}$ ) and  $15^\circ$  ( $\text{RbC}_{24}$ ). These local maxima can be guessed in the photographic data at room temperature; they grow in intensity as  $T$  is reduced and are precursor effects of the primary incommensurate peaks which appear at the liquid-solid transitions. In the case of  $\text{RbC}_{24}$  a comparison with the anisotropic  $S(q)$  calculated via molecular dynamics as shown in Fig. 9 is very satisfactory, and the broad maxima at  $\pm 15^\circ$  (+ and - relate to the two equivalent domains) are clearly revealed in the simulation. However, these maxima are absolute maxima of intensity for the halo, while in the experimental data they appear only as shoulders and the maximum intensity is actually at  $\varphi = 30^\circ$ . It seems indeed that the MD simulation would correspond to a slightly lower effective temperature as compared with our room-temperature results. For the secondary halo centered about  $(10.0)_G$  scans similar to

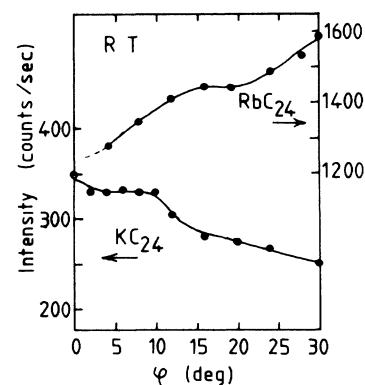


FIG. 8. Maximum intensity on the central halo as a function of the angle  $\varphi$  from  $0^\circ$  to  $30^\circ$ , showing the opposite behaviors of  $\text{KC}_{24}$  (maximum at  $0^\circ$ ) and  $\text{RbC}_{24}$  (maximum at  $30^\circ$ ). Local broad maxima are precursors of the low- $T$  peaks for the ordered states.

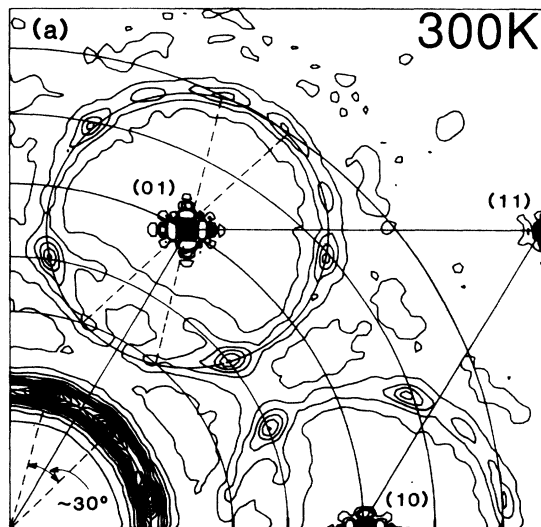


FIG. 9. Simulated structure factor  $S(q)$  for Rb in stage-2 GIC's at 300 K as obtained from molecular-dynamics simulation, by Fan *et al.* (Ref. 14). The contour plot shows a good overall agreement with the present data.

those of Fig. 8 were performed as a function of  $\mu$  (defined in Fig. 4) instead of  $\varphi$ . Similar intensity variations were observed, namely decrease and increase of the intensity with  $\mu$  for  $\text{KC}_{24}$  and  $\text{RbC}_{24}$ , respectively, and intensity maxima at  $\mu=0^\circ$  ( $\text{KC}_{24}$ ) and  $\mu=30^\circ$  ( $\text{RbC}_{24}$ ). Compared to the primary halo the diffuse scattering is here weaker by about 2.2 for  $\text{KC}_{24}$  and 3.2 for  $\text{RbC}_{24}$ .

## V. LOW-TEMPERATURE PHASE TRANSITIONS

As the temperature is decreased from room temperature the diffuse scattering intensity in the halos described previously concentrates progressively in both the radial and angular directions. For the radial direction this is illustrated in Fig. 10, where the width (half width at half maximum) of the principal central halo is plotted versus

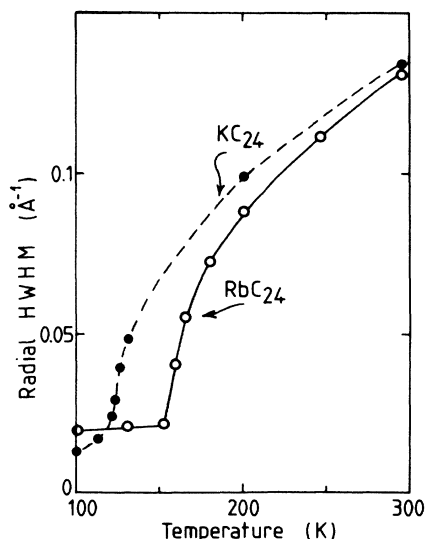


FIG. 10. Temperature dependence of the width (HWHM) of the primary halo, at  $q_1$ , in the liquid phase for  $\text{KC}_{24}$  and  $\text{RbC}_{24}$ .

temperature. The width is derived from radial scans of this halo across the position of the primary (10,0) reflection of the low-temperature AM solid phase. The HWHM decreases more and more rapidly as the transition temperature  $T_c$  from the liquid to the solid phase is approached. Similar behaviors are observed for  $\text{KC}_{24}$  and  $\text{RbC}_{24}$  and a saturation of the width limited by the experimental resolution occurs below  $T_c$ . Actually at  $T_c$  the diffuse scattering in the halos vanishes and one obtains sharp reflections either in the  $(hk,0)$  plane or in the corresponding  $(hk,l)$  reciprocal (r.l.) rows. These reflections obey the extinction conditions given by the stacking sequence of the intercalate layers.

We recall here the main characteristics of the diffraction pattern from the ordered phase as it appears below  $T_c$ , in an intermediate temperature range, above the lower temperature effects (i.e., above  $T \sim 100$  K). As shown in Fig. 11 it is composed of the following.

(i) A primary hexagonal r.l. rotated with respect to the

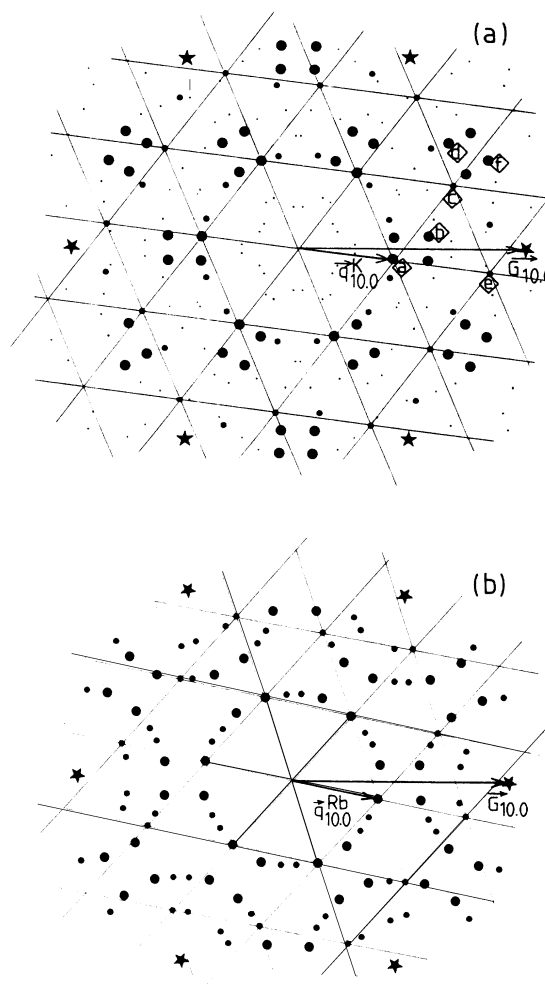


FIG. 11. Schematic drawings of the  $(hk,0)$  reciprocal lattices (r.l.) of  $\text{KC}_{24}$  (a) and  $\text{RbC}_{24}$  (b). They are composed of a basic hexagonal lattice defined by  $\mathbf{q}_{10,0}^{\text{K}}$  or  $\mathbf{q}_{10,0}^{\text{Rb}}$  (outlined) and the satellites produced by the shortest graphite r.l. vectors. The symmetrical twin lattice is also shown. The size of the dots reflects the relative intensities of the associated reflections.

graphite r.l. and defined by  $\mathbf{q}_{10,0}^K$  (or  $\mathbf{q}_{10,0}^{Rb}$ ). The modulus of  $\mathbf{q}_{10,0}$  and its rotation  $\theta$  relative to  $\mathbf{G}_{10,0}$  depend on the nature of the AM, its in-plane density, and the stage of the GIC.

(ii) Satellite reflections with r.l. vectors of the type  $\mathbf{q} + \mathbf{G}$ , where  $\mathbf{q}$  and  $\mathbf{G}$  are general r.l. vectors of the AM and graphite host, respectively. The satellite reflections are a manifestation of the graphite modulation.

(iii) Significant intensity is observed for the shortest r.l. vectors only, both for the primary and modulation-induced reflections. It implies that large atomic displacement from the ideal AM and graphite lattice sites are involved.

Furthermore, it is known<sup>16,21</sup> that the intercalate layers are stacked according to an  $\alpha\beta\gamma$  rhombohedral stacking scheme. This is deduced from the fact that the AM reflections obey the selection rule  $-h+k+l=3n$  ( $n$  an integer). It is important to realize that the rhombohedral stacking of the AM layers is not directly related to that of the graphite. This is so because successive AM and graphite layers are related by translations  $\frac{2}{3}\mathbf{a}_{AM} + \frac{1}{3}\mathbf{b}_{AM} + \frac{1}{3}\mathbf{c}$  and  $\frac{2}{3}\mathbf{a}_G + \frac{1}{3}\mathbf{b}_G + \frac{1}{3}\mathbf{c}$ , respectively, whose in-plane components are incommensurate. This point does not seem to have been clearly understood in some previous works.

We now present in-plane and out-of-plane intensity data about (i) the AM main and satellite reflections near and below the AM ordering (liquid-solid) transition (Sec. V A) and (ii) the distinct low-temperature behaviors of the K and Rb GIC's (Sec. V B).

#### A. Liquid-solid transition

Beginning with  $KC_{24}$ , Fig. 12 shows the temperature dependence of the peak intensity for the K primary reflection at  $\mathbf{q}_{10,1}^K$  [Fig. 12(a)] and the closest modulation satellite at  $-\mathbf{q}_{10,1}^K + \mathbf{G}_{10,1}$  [Fig. 12(b)].

Note that the primary reflection occurs for  $l=1$  [the  $(10.0)_K$  reflection is absent] while the satellite lies in the  $(hk.0)$  plane. Despite the small number of data points (the broken lines are only guides to the eye) it appears that extrapolating the intensity yields a transition temperature  $T_c = 124 \pm 1$  K, for both reflections. There is, however, an apparently different behavior near  $T_c$  since the buildup of the intensity is more abrupt for the satellite reflection than for the primary one. This may be the signature of different precursor critical phenomena, but it more likely reflects the interplay with stacking faults which occurs for the primary reflection only, as shown below.

Figure 13 shows scans along  $l$  for the same primary [part (a)] and satellite [part (b)] reflections. Above  $T_c$  (scans at 132 and 127 K) the intensity is constant with  $l$  (the decrease of the scattering factors with  $q$  is negligible here) and it increases as  $T$  is lowered because of the progressive concentration of the diffuse scattering from the halos towards the main- and satellite-reflection positions. For the primary reflection [Fig. 13(a)] at  $T_c$  (124 K) a broad hump appears centered at  $l=1.5$ . It then splits in two maxima which can be interpreted as resulting from two overlapping broad peaks centered at  $l=1$  and 2. For

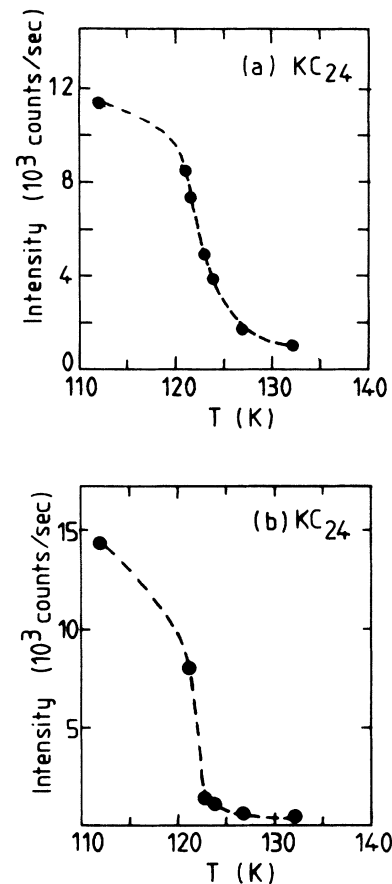


FIG. 12. Temperature dependence of the peak intensity for the primary reflection at  $\mathbf{q}_{10,1}^K$  (a) and the modulation satellite reflection at  $-\mathbf{q}_{10,1}^K + \mathbf{G}_{10,1}$  (b) in  $KC_{24}$  near the liquid-solid transition ( $T_c \sim 124$  K).

a well-ordered rhombohedral  $\alpha\beta\gamma$  stacking, sharp peaks would occur at  $l=1$  and 2 and the broadening can be therefore attributed to the presence of stacking faults. Similar observations were made by Hastings *et al.*<sup>21</sup> on HOPG samples and, as they pointed out, this broadening is comparable to that of the graphite  $(10.l)$  reflections [see for instance the overlap of the  $(10.4)$  and  $(10.5)$  reflections in Fig. 3(a)]. It strongly suggests that the stacking faults of the graphite host are transferred to the AM layer stacking. Moreover, turning to Fig. 13(b) one sees sharp peaks at  $l=0$  and  $l=3$  for the scan corresponding to the modulation satellite. This selection rule is in agreement with the definition of the satellite wave vector  $(-\mathbf{q}_{10,l}^K + \mathbf{G}_{10,l})$  and the combination of the rhombohedral selection rules for the AM and graphite sublattices which gives  $l=3n$  ( $n$  an integer). Since these particular satellite reflections are sharp [their width is on the order of that of the graphite  $(00.l)$  reflections], they are not affected by the graphite stacking faults. This observation is actually related to the fact that in any hexagonal- or rhombohedral-layer stacking based on the  $A, B, C$  scheme the stacking faults affect the  $h-k \neq 3n$  reflections while the  $h-k = 3n$  reflections are independent of the particular stacking sequence, either ordered

or disordered. In the present case where we are dealing with a main AM lattice incommensurate with the graphite, the absence of a stacking-fault effect for the satellite reflection can only be understood if the K atoms from different layers are related by vectors such as  $(0,0)$ ,  $(\frac{1}{3}, \frac{2}{3})$ , or  $(\frac{2}{3}, \frac{1}{3})$  relative to the *graphite* unit vectors. This condition is satisfied if the K atoms are arranged as follows. (i) The K atoms form layers characterized by a primitive hexagonal lattice incommensurate with the graphite one. (ii) The layers are stacked rhombohedrally in an  $\alpha\beta\gamma$  sequence (where  $\alpha$ ,  $\beta$ , and  $\gamma$  refer to the incommensurate K hexagonal lattice sites). (iii) The K atoms are relaxed to the (closest) graphite honeycomb-lattice sites. The latter appears to be a necessary condition for the sharpness

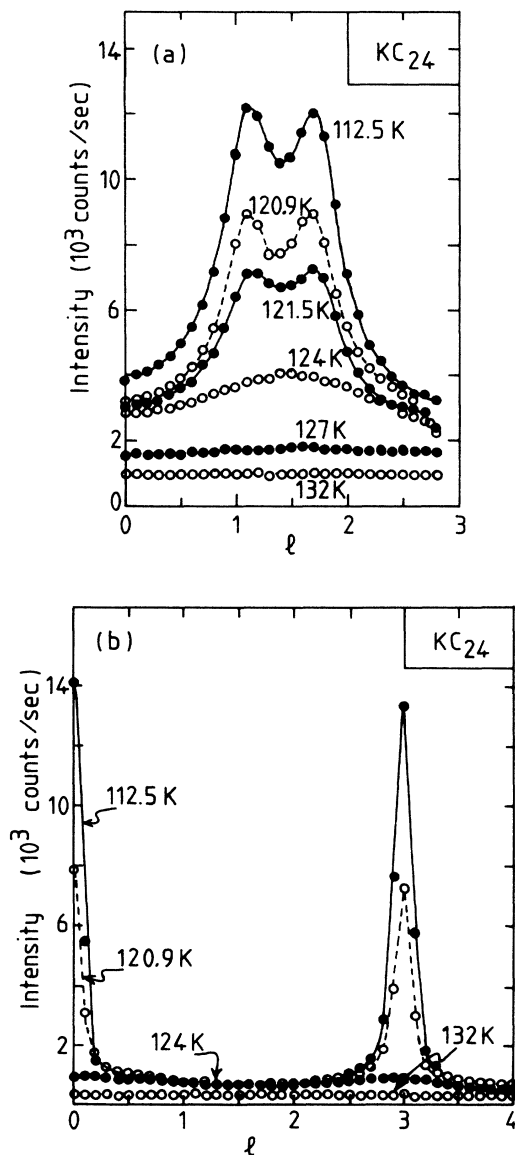


FIG. 13. Scans along  $l$  through the primary (a) and satellite (b) reflections defined in Fig. 12, in  $\text{KC}_{24}$ , for selected temperatures close to  $T_c \sim 124$  K. The growth of the intensity modulations corresponds to the establishment of out-of-plane order. The lines are guides for the eye.

along  $l$  of the satellite peaks in Fig. 13(b). We recall that the *ad hoc* parameter used in Sec. III B to account for the contribution of the K atoms to the graphite reflection intensities yields 57% of registered atoms at room temperature and 86% at 12 K. We shall return to this important point in Sec. VI.

Coming back to the temperature dependence of the peak intensities in Fig. 12, it is seen that because of the stacking-fault effects the main reflection at  $q_{10,1}^{\text{K}}$  is not appropriate to probe the order parameter through the transition. In this respect the temperature dependence of the satellite reflection intensity in Fig. 12(b) is more representative of the in-plane ordering.

In the case of  $\text{RbC}_{24}$  we present in Figs. 14 and 15 similar type of data about the main and satellite reflections for the ordering transition at  $T_c \approx 156$  K. In Fig. 14 their peak intensity is given between room temperature and 10 K. Both main and satellite reflections show a progressive buildup of the intensity below  $T_c$ , indicating a continuous transition. However, because of the presence of defects in the crystals (such as a high stacking-fault concentration), it is not possible to draw

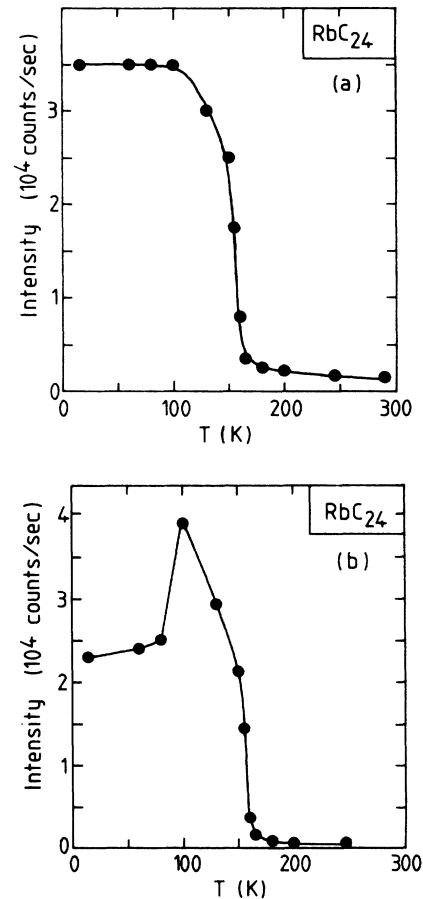


FIG. 14. Temperature dependence of the peak intensity for the primary reflection at  $q_{10,1}^{\text{Rb}}$  (a) and the modulation satellite reflection at  $-q_{10,1}^{\text{Rb}} + G_{10,1}$  (b) in  $\text{RbC}_{24}$  (similar to Fig. 12 for  $\text{KC}_{24}$ ). The liquid-solid transition occurs at  $T_c \sim 156$  K. The abrupt decrease below 100 K comes from changes in the inter-layer correlations.

conclusions about the order of the transition. In any case we expect the transition to be intrinsically continuous (not due to defects), in agreement with both quasielastic neutron scattering<sup>17</sup> and molecular-dynamics<sup>14</sup> studies. While the intensity saturates below 100 K for the main reflection, the satellite shows a dramatic decrease at the same temperature, and this is associated with a change of the Rb interlayer ordering, as will be discussed in Sec. VB.

Figure 15 displays scans along  $l$  for the same r.l. rows between 160 and 130 K. For the main reflections [Fig. 15(a)], at 160 K, broad peaks emerge from the diffuse streaks characteristic of the high-temperature 2D liquid. They are centered at about  $l=1.5$  and 4.5, which indicates a tendency for an  $\alpha\beta\alpha\beta$  stacking of the Rb layers. Then, beginning at 155 K these maxima develop a composite structure consisting mainly of overlapping peaks at  $l=1, 2, 4$ , and 5. As in  $\text{KC}_{24}$ , this agrees with a rhombohedral  $\alpha\beta\gamma$  stacking sequence of the Rb layer (again

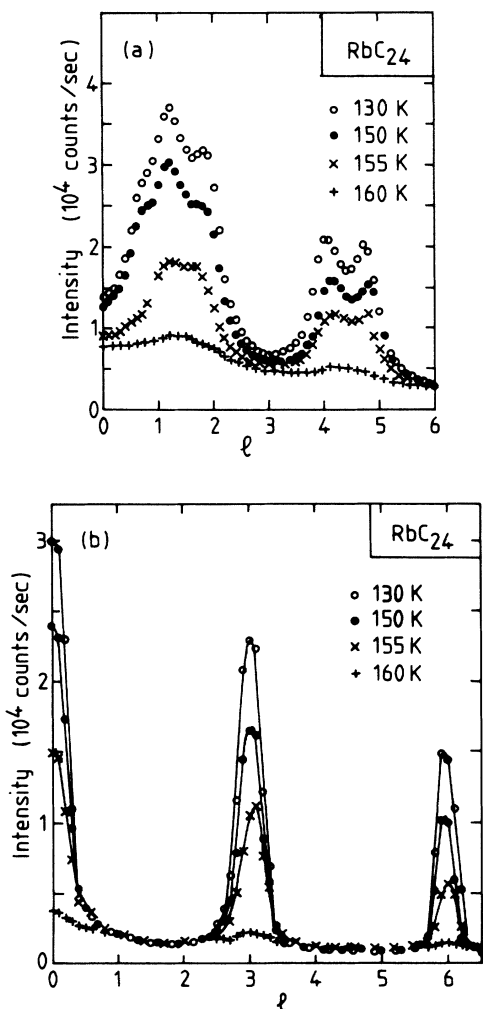


FIG. 15. Scans along  $l$  through the primary (a) and satellite (b) reflections defined in Fig. 14, in  $\text{RbC}_{24}$ , for selected temperatures close to  $T_c \sim 156$  K. As in  $\text{KC}_{24}$  (Fig. 13), sharp and well positioned peaks are observed for the satellite reflection while the main reflections reveal broad overlapping peaks.

we emphasize that  $\alpha, \beta$ , and  $\gamma$  refer to the main Rb lattice, incommensurate with the graphite). However, a supplementary peak at  $l \sim 1.2$  develops at 150 and 130 K, and this is evidence for a distinct type of stacking which is not identified. Note that no such peak is observed near  $l \sim 4.2$ , contrary to what one would expect from the r.l. periodicity.

For the r.l. row that corresponds to the satellite reflections the behavior is very similar to that of  $\text{KC}_{24}$  with relatively sharp peaks for  $l=3n$ . Similarly we suggest that stacking faults originating from the graphite host broaden the diffraction peaks of the main Rb reflections while they have no influence on the modulation-induced satellite reflections. As in  $\text{KC}_{24}$  it strongly supports the view that most Rb atoms are actually registered, i.e., at or very close to the graphite hexagon centers.

### B. Evolution of the AM order below 100 K

Compared to the liquid-solid transition the supplementary changes that occur at lower temperature have received much less attention and their description has led to conflicting reports, partly because of their complexity. This is the case for the low-temperature phase transition at  $T_L \sim 95$  K in  $\text{KC}_{24}$  which was first studied by Parry and Nixon<sup>18</sup> and associated with a change in the stacking. A similar observation was reported by Hastings *et al.*,<sup>21</sup> who also found that the transition was first order. In our previous photographic studies,<sup>7-9</sup> we observed that the transition also involves intralayer effects because of the formation of a complex  $(hk.0)$  diffraction pattern produced by the splitting of the main  $K$ -lattice reflections into three components and the subsequent modulation effects. This was interpreted as being due to a decrease of the symmetry of the  $K$  layer from hexagonal to oblique with a unit cell defined by  $a_L = 6.10$  Å,  $b_L = 5.81$  Å,  $\gamma_L = 124.14^\circ$ , the  $a_L$  axis being rotated off  $a_G$  by  $9.12^\circ$ .<sup>8</sup> Because of the low symmetry of this lattice, six equivalent domains coexist, and introducing first-order modulation satellites ( $\{\mathbf{G}_{100}\}$  wave vectors only), one obtains an intricate  $(hk.0)$  pattern that corresponds very nicely to the observed diffraction pattern, as shown in Fig. 16.

More recently a different interpretation of the diffraction pattern in terms of a fragmentation into multiple high-order commensurate superlattices has been suggested by Winokur and Clarke.<sup>30</sup> It makes use of devil's-staircase arguments proposed in particular by Mitani and Niizeki.<sup>36</sup> While it is elegant, we believe that this interpretation does not apply because it is based on  $(hk.0)$  x-ray diffraction contour maps (Fig. 1 of Ref. 30) whose resolution is lower than that of the stationary photograph we reproduce here so that they give an erroneous description of the reciprocal lattice. As an example, the group of spots labeled 1,2,3,8 or the 9,10,11,12 group in Fig. 16(b) is not resolved in the contour map of Winokur and Clarke. On the contrary, the single oblique lattice defined above accounts for the position of all observed reflections.

This is further confirmed by the present study, as we

were able to perform diffractometer  $l$  scans at 12 K along r.l. rows corresponding to the  $(hk.0)$  points labeled 1–6 (main K reflections) and 9–13 (satellite reflections) in Figs. 16(b). Actually these reflections belong to different domains. However, since the domains are equivalent by symmetry it is justified and more convenient to refer these reflections to a unique r.l. setting using the appropriate symmetry operations of the graphite lattice. It allows us to index the scans presented in Fig. 17 according to the equivalent r.l. row for this particular setting. These scans exhibit intensity modulations which can be analyzed as follows, in terms of interlayer correlations. Let us consider first the main reflections. In Fig. 17(a) the  $(10.l)$  and  $(01.l)$  scans show well-defined peaks centered at  $l=1.5$ , while the  $(11.l)$  and  $(\bar{1}1.l)$  scans (though the latter does not extend fully to  $l=4$ ) show similar peaks centered at  $l=0$  and 3. For  $(\bar{2}1.l)$  and  $(\bar{1}2.l)$  the intensity is weaker by one or two orders of magnitude and the profiles are less well defined. However, there is evidence for intensity maxima near  $l=1, 2$ , and 4 [Fig. 17(b)]. Comparing to the scans along  $l$  of the main and satellite reflections above  $T_L$ , as described in Fig. 13, it is clear that a drastic change of the correlations between the K layers accompanies the in-plane hexagonal-oblique

transition at  $T_L$ . While the  $(10.l)$ ,  $(01.l)$ ,  $(11.l)$ , and  $(\bar{1}1.l)$  profiles appear to indicate a stacking sequence which involves two K layers in an  $\alpha\beta$ -type stacking, the remaining  $(\bar{2}1.l)$  and  $(\bar{1}2.l)$  profiles would rather support a three-layer period of the type  $\alpha\beta\gamma$  (the stacking vector between  $\alpha$ ,  $\beta$ , and  $\gamma$  is not specified here). One way to reconcile these distinct types of interlayer correlations would be to consider a stacking sequence consisting of six K layers and represented schematically as  $\alpha\beta\alpha'\beta'\alpha''\beta''$ . Parry and Nixon<sup>18</sup> and Hastings *et al.*<sup>21</sup> in their study of HOPG samples also came to the conclusion that the stacking involves six K layers at low temperature. As in these early works, we have failed to derive the precise relation between the successive K layers, i.e., the stacking vector, to account consistently for the selection rules displayed by all scans in Figs. 17(a) and (b). The origin of this complexity, which bears resemblance to similar difficulties encountered with  $\text{RbC}_{24}$  (see below) is not yet identified.

Turning to the  $l$  scans for the satellite reflections (obtained using the  $\{\mathbf{G}_{10,0}\}$  graphite wave vectors only), Figs. 17(c) and (d) show some representative intensity profiles. They are indexed according to the main K reflections from which they originate.  $(10.l)_M$  and  $(01.l)_M$  show peaks at  $l=0$  and 3,  $(\bar{1}1.l)_M$  has a peak

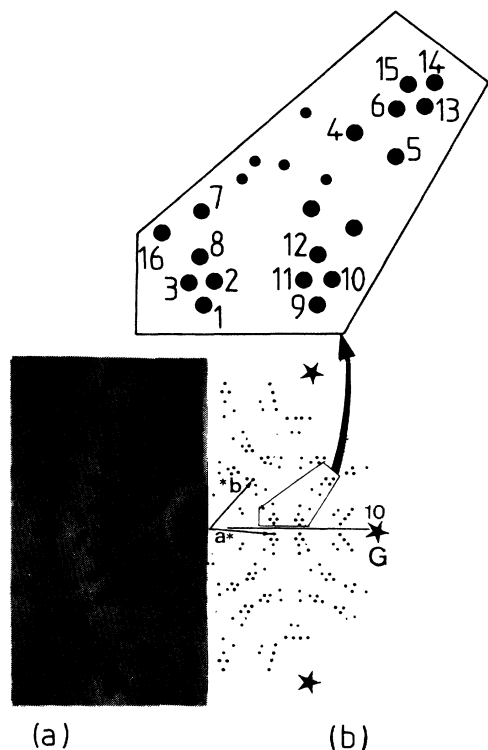


FIG. 16. Left (a) is a portion of a monochromatic Laue photograph from a  $\text{KC}_{24}$  single crystal in the low-temperature phase.  $\text{Cu K}\alpha$  x-ray radiation and a cylindrical camera have been used. Right (b) gives a drawing of the reciprocal lattice obtained with a unique oblique 2D lattice (plus the symmetry-induced twins). The comparison between the observed and simulated patterns is satisfactory. The inset shows an enlarged portion of the simulated pattern where selected r.l. peaks are numbered.

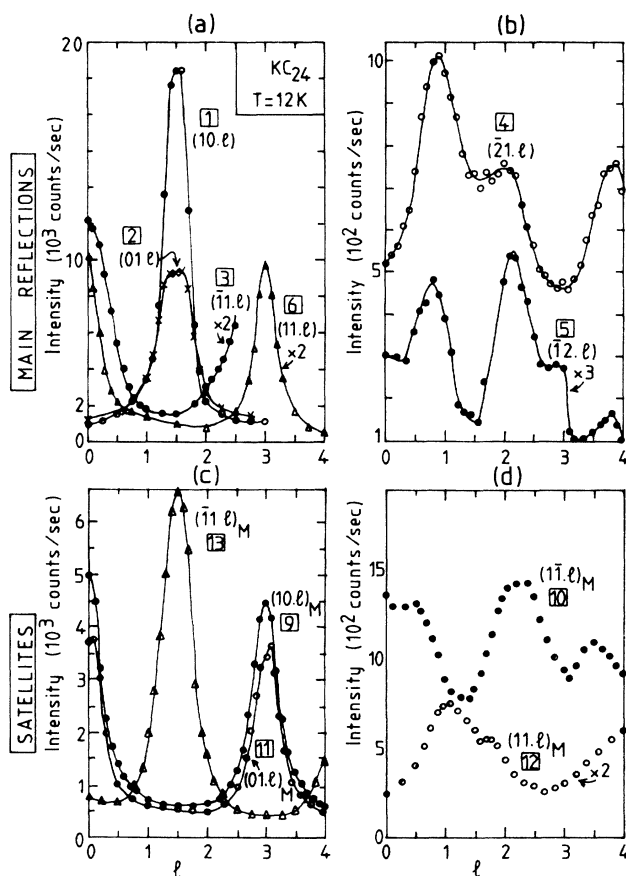


FIG. 17. Scans along  $l$  of selected main (a) and (b) and satellite (c) and (d) reflections in  $\text{KC}_{24}$  at  $T=12$  K. The reflections are numbered (in square boxes) according to Fig. 16.

centered at  $l=1.5$ , while the weaker  $(11.l)_M$  and  $(\bar{1}\bar{1}.l)_M$  intensity profiles show modulations which are less well defined. Using only the main and satellite reflections which are strong and well defined one can express their selection rules as follows:

|                    | Main reflections       | Satellite reflections  |
|--------------------|------------------------|------------------------|
| 10.l               | $l = 3n + \frac{3}{2}$ | $l = 3n$               |
| 01.l               | $l = 3n + \frac{3}{2}$ | $l = 3n$               |
| 11.l               | $l = 3n$               |                        |
| $\bar{1}\bar{1}.l$ | $l = 3n$               | $l = 3n + \frac{3}{2}$ |

These selection rules imply a stacking sequence of the type

$$A\alpha AB\beta BC\alpha' CAB' AB\alpha'' BC\beta'' C ,$$

where the  $\alpha$  and  $\beta$  layers are centered with respect to each other, i.e., related by a translation  $\frac{1}{2}\mathbf{a}_L + \frac{1}{2}\mathbf{b}_L$  ( $a_L$  and  $b_L$  refer to the oblique cell defined before). Moreover, the selection rules are not the same for a main reflection and its satellite which shows that the modulation wave vector has a  $c^*$  component. This is in fact expected because of the ordered stacking of the graphite layers, however, one would normally have a  $c^*$  component of  $\pm 1$  for the modulation wave vector given the rhombohedral stacking of the graphite layers. In contrast, it appears that the observed selection rules for the satellite reflections yield a  $c^*$  component of  $\pm \frac{3}{2}$ . This would suggest that the period of the modulation potential corresponds to two K layers, for instance from  $\alpha$  to  $\alpha'$  in the stacking sequence listed above. This is difficult to account for because the graphite bounding layers of the  $\alpha$  and  $\alpha'$  layers are different, namely  $A$  and  $C$ , respectively (we recall that the graphite stacking is not modified in the temperature range considered here). The problem of the exact stacking of the K layer and in particular the nature of the stacking vector which transforms  $\alpha\beta$  into  $\alpha'\beta'$  and then  $\alpha''\beta''$  are not understood yet.

In the case of  $\text{RbC}_{24}$  the situation appears more simple at first because the symmetry of the in-plane intercalant structure remains hexagonal to the lowest temperature.<sup>36,37,8,9</sup> However, the  $(hk.0)$  diffraction pattern is modified as the temperature is reduced because of the growth of higher-order modulation satellites. It was shown previously<sup>8</sup> that one has to take account of satellites defined by wave vectors such as  $\{\mathbf{G}_{10,0}\}$ ,  $\{\mathbf{G}_{11,0}\}$ , and  $\{\mathbf{G}_{20,0}\}$  in order to fit the low-temperature  $(hk.0)$  diffraction pattern, which indicates that the corresponding coefficients of the modulation potential increase as  $T$  decreases. In Fig. 18 such a simulated diffraction pattern is shown where the full hexagonal symmetry resulting from domain coexistence is displayed. It compares well with the observed monochromatic Laue patterns taken at 25 K [see Fig. 6(a) in Ref. 8], especially as most of the predicted r.l. points correspond to observed reflections of appreciable intensity.

While no drastic change is thus taking place inside the Rb layers, it is known from previous studies that their stacking order undergoes one modification, at least, below the liquid-solid transition. This is first evidenced

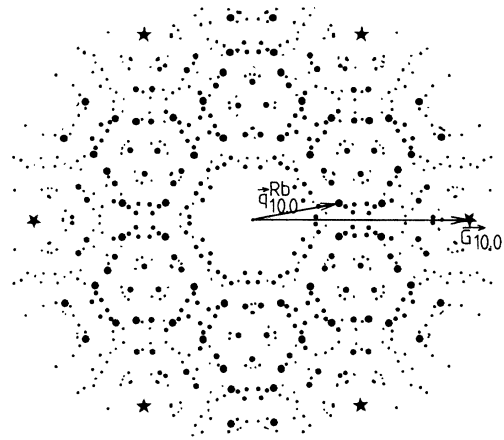


FIG. 18. Simulated  $(hk.0)$  pattern obtained from a primary hexagonal lattice defined by  $\mathbf{q}_{10,0}^{\text{Rb}}$  and satellites produced by wave vectors of the type  $\{\mathbf{G}_{10,0}\}$ ,  $\{\mathbf{G}_{11,0}\}$ , and  $\{\mathbf{G}_{20,0}\}$ . Symmetry-induced twins (domains) are also taken into account. This simulation agrees well with the low-temperature diffraction pattern of  $\text{RbC}_{24}$ .

by the observation of resistive<sup>38,39</sup> and specific-heat anomalies<sup>40</sup> among which the 106 K one was attributed to a change of the stacking order. Neutron studies on HOPG samples of the scattering along  $l$  for selected r.l. rows showed that the stacking period is at least tripled below  $T_L = 106$  K,<sup>31,37</sup> and a possible model was proposed to account for several characteristics of the corresponding  $l$  scans, although some discrepancies remained.<sup>24</sup>

We have also studied the temperature dependence of several main and satellite reflections down to 15 K. In particular we scanned the  $(10.l)$  (main) and  $(10.l)_M$  (modulation satellite) reflections presented already in Figs. 14 and 15. Figure 19(a), for the  $(10.l)$  main reflections reveals various changes in the intensity profiles. First, while the scans at 130 K [Fig. 15(a)] and 100 K are quite similar and reflect primarily a tendency for a faulted  $\alpha\beta\gamma$  rhombohedral stacking of the Rb layer, the profile at 80 K shows the growth of several peaks whose  $l$  values are impossible to determine because of the important overlap between the peaks. Overall this profile much resembles that obtained by Suzuki *et al.*<sup>31</sup> on HOPG at  $T=10$  K, although the width of the peaks is larger in our case because of larger stacking-fault effects. Along with these authors we attribute the observed change of the profile to the establishment of a long stacking period which cannot be identified. On further cooling ( $T=60$  and 15 K) the peaks broaden and overlap even more. This appears to be related to the behavior of the  $(10.l)_M$  satellite reflections presented in Fig. 19(b), which shows a sudden decrease of the peak intensity below 100 K associated with a broadening of the peaks centered at  $l=3n$  and a progressive growth of the intensity between the peaks, when the temperature is lowered. The decrease of the peak intensity is also clearly revealed in Fig. 14(b).

These effects indicate successive changes in the stacking order and the interlayer correlations beginning below

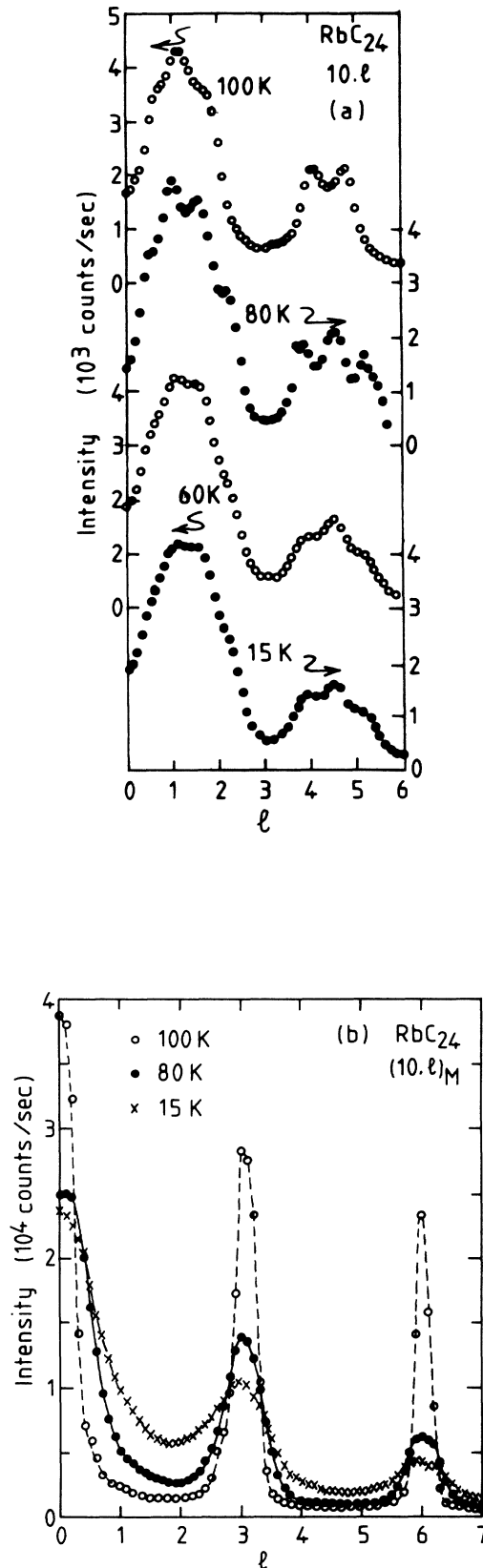


FIG. 19. Same scans as on Fig. 15 for  $\text{RbC}_{24}$  but at lower temperatures. They reveal [in particular those of the modulation satellite in (b)] a tendency of the intercalate layer stacking to deteriorate at low temperature.

100 K and they correspond undoubtedly to the transition at 106 K reported previously.<sup>37-39</sup> The difference in temperature may be due to various factors, among which the crystallinity and the stacking faults of the graphite matrix are probably important ones (our single-crystal samples were of course free from the orientational disorder of the HOPG samples studied previously, but they presented a high stacking-fault concentration). While the evolution of the stacking order of the Rb layers is difficult to analyze in details, the final low-temperature state clearly shows a progressive loss of the interlayer correlations. Such an effect is obviously unexpected in normal systems where one expects a better ordering at the temperature is reduced. However, similar behaviors have been observed in other GIC's such as in Cs stage-2 and especially stage-3 compounds<sup>28</sup> and also in stage-2  $\text{C}_8\text{Br}$ .<sup>38</sup> In all cases the origin of this "anomalous" effect certainly lies in the competition between intralayer and interlayer correlations. As the temperature decreases, the influence of the graphite bounding layers on the intercalant atoms increases, but if both sublattices remain incommensurate, there is a conflict between the tendency of the intercalant layers to adopt a stacking sequence which minimizes their electrostatic and elastic interactions and the particular stacking of the graphite sublattice. This interesting type of frustration would deserve to be studied theoretically.

## VI. STRUCTURAL MODEL FOR THE LOW-TEMPERATURE PHASES OF $\text{KC}_{24}$

As indicated in Sec. I, the understanding of the structure of the AM layers at low temperature is still debated for two main reasons: (i) the existence of different models and (ii) the lack of extensive and reliable intensity data to distinguish between them. The case of  $\text{KC}_{24}$  is probably the most controversial because of the hexagonal-oblique symmetry change at  $T_L = 95$  K and the difficulty to use a discommensuration-domain description owing to the small size of the constituting domains which are involved. This justifies that further efforts be made to clarify these issues, and in the present case we have worked out a structural model which provides a reasonably fair fit to our new intensity data, above  $T_L$ . This model has also been applied to the low-temperature oblique structure below  $T_L$ , but in this case further difficulties arise as we do not have a good understanding of the K layer stacking sequence.

The model is actually extended from Diczko's,<sup>29</sup> as described now. For the intermediate phase above  $T_L$ , we assume that the K layers, which are sandwiched between identical graphite layers, consist of K atoms which form a close-packed 2D hexagonal lattice defined by the K primary wave vector  $\mathbf{q}_{10,0}^K$ . It leads to lattice parameters  $a_K, b_K$  as follows:

$$a_K = b_K = 4\pi / (\sqrt{3} \mathbf{q}_{10,0}^K) = 5.80 \text{ \AA} .$$

This lattice is incommensurate with graphite and is rotated with respect to the graphite lattice by the observed angle between  $\mathbf{q}_{10,0}^K$  and  $\mathbf{G}_{10,0}$ , or  $7.5^\circ$ . This rotation can

be introduced, equivalently, in one direction or the other,  $+7.5^\circ$  or  $-7.5^\circ$ , leading to twinning. Apart from the orientation, the relative position of the K layer and the graphite bounding layers is, of course, arbitrary since their lattices are incommensurate. The second step consists in laterally shifting each K atom towards the nearest hexagon center of the graphite honeycomb lattice. In other words, the K atoms become centered with respect to the facing carbon hexagons of the graphite bounding layers. This displacement scheme favors the short-range K-C interaction and can be viewed as a crude way to introduce the influence or modulation of the graphite sublattice onto the K one through a "relaxation" of the K lattice. It leads to registry, in agreement with the conclusions drawn in Sec. V from the profiles of the main and satellite reflections along  $c^*$ .

Figure 20 shows a typical distribution of K atoms obtained using the above procedure. It is represented on a piece of graphite honeycomb lattice in the shape of a losange (the C atoms are at the vertices of the hexagons). The losange contains  $31 \times 30$  hexagons, giving a size of  $76 \times 73.5 \text{ \AA}^2$ , and 173 K atoms. It corresponds to a C/K ratio of 10.75 so that for a stage-2 compound, one obtains a formula  $\text{KC}_{21.5}$ . From the analysis of Fig. 20 one sees that each K atom is surrounded by six first neighbors (as in the starting hexagonal K lattice) at distances of  $2a_G$ ,  $\sqrt{7}a_G$  or  $3a_G$ . We note that, contrary to the basic principle of the discommensuration-domain model, no  $\sqrt{7} \times \sqrt{7}$  domains are formed. Instead one can isolate small groups of K atoms which form  $2 \times 2$  clusters. To test the validity of this model we have calculated the intensities of six reflections (three main and three satellite reflections). Following Mori *et al.*,<sup>27</sup> these reflections are labeled *a*, *b*, *c*, *d*, *e*, and *f* and they are indicated in Fig. 11(a). For the calculation one needs to consider the full 3D structure of the K sublattice. We recall that the stacking sequence above  $T_L$  is represented by  $A\alpha AB\beta BC\gamma C$  and we point out again that the face-centered cubic (fcc), i.e.,  $\alpha\beta\gamma$  stacking of the K layers is distinct from that of the graphite layers (*A*, *B*, *C*) because of their relative in-plane incommensurability. In other words, the in-plane shifts associated with these stackings are incommensurate.

Following Diczno<sup>29</sup> we build the three-layer stack of potassium layers starting from a fcc stack of 2D hexagonal incommensurate lattices as defined above (before the relaxation process). Then the K atoms are displaced or

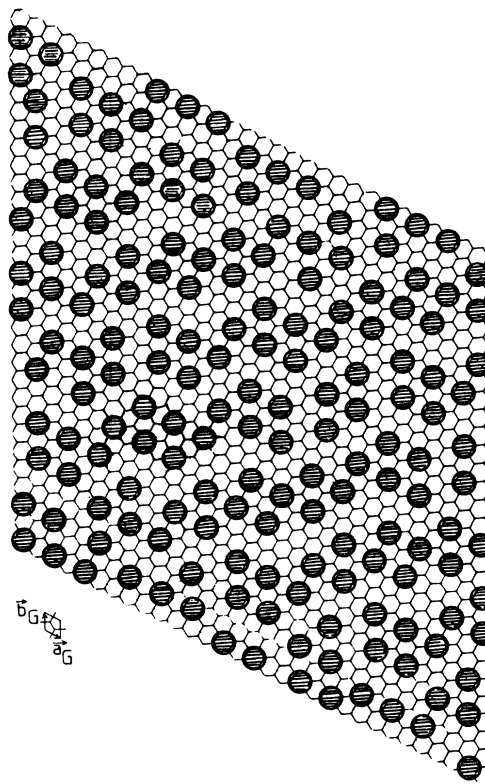


FIG. 20. Model of the K atoms distribution obtained after "relaxation" of an incommensurate hexagonal lattice on a graphite honeycomb layer. The ratio number of carbon atoms divided by the number of potassium atoms is about 10.75. No evidence is found for  $\sqrt{7} \times \sqrt{7}$  domains.

relaxed towards the nearest favorable site (hexagon center) of the corresponding graphite bounding layers, which are either of the *A/A*, *B/B*, or *C/C* type. By this process the three K layers correspond to an average lattice which is a fcc (or  $\alpha\beta\gamma$ ) stacking of hexagonal 2D lattices. However, the relaxation being referred to different graphite bounding layers (*A/A*, *B/B*, or *C/C*), the K distribution differs in the three layers.

The structure factors were calculated by summation over all K atoms in the three-layer model. We found that the results become independent of the size of the model layer when it is on the order of the losange in Fig. 20 or about  $30a_G \times 30a_G$  or  $75 \text{ \AA} \times 75 \text{ \AA}$ . In Table I, the calcu-

TABLE I. Comparison of observed and calculated intensities for three main and three satellite reflections as a function of  $R_0$  which characterizes the partial relaxation of the K atoms. Lorentz-polarization corrections were applied to the observed intensities.

| Index as in<br>Mori <i>et al.</i> (Ref. 25)<br>and Fig. 11(a) | <i>(hk)</i> indices of<br>the reflections | $I_{\text{obs}}$ | $I_{\text{calc}}$<br>$R_0=0$ | Intensities [arbitrary units, $I(b)=100$ ]  |  |   |  |
|---|---|------------------|------------------------------|---|--|---|--|
|   |   |                  |                              | $I_{\text{calc}}$<br>$R_0=0.02 \text{ \AA}$ | $I_{\text{calc}}$<br>$R_0=0.035 \text{ \AA}$ | $I_{\text{calc}}$<br>$R_0=0.05 \text{ \AA}$ | $I_{\text{calc}}$<br>$R_0=0.1 \text{ \AA}$ |
| <i>a</i>  | $(10)_K$                                  | 21               | 0                            | 5.6   | 6.7  | 7.9   | 14.3                                       |
| <i>b</i>  | $(10)_K + (10)_G$                         | 100              | 100                          | 100   | 100  | 100   | 100  |
| <i>c</i>  | $(11)_K$                                  | 22               | 18.3                         | 21.1  | 24.3   | 36.5  | 87.8                                       |
| <i>d</i>  | $(11)_K + (01)_G$                         | 18.5             | 0                            | 4.6   | 4.8  | 4.9   | 5.1  |
| <i>e</i>  | $(20)_K$                                  | 4.3              | 0                            | 1.1   | 2.1  | 3.5   | 13.5                                       |
| <i>f</i>  | $(11)_K + (10)_G$                         | 8.3              | 0                            | 4.5   | 5.0  | 5.2   |  |

lated intensities have been obtained with models of  $50a_G \times 50a_G$  or  $120 \text{ \AA} \times 120 \text{ \AA}$  containing about 500 K atoms.

According to the selection rules on  $l$  for the main and satellite reflections, it turns out that two of the six reflections ( $b$  and  $c$ ) correspond to  $l=0 \pmod{3}$ ; they are called "in-plane," while the others correspond to  $l=\pm 1 \pmod{3}$  and are therefore "out of plane." However, some of the out-of-plane reflections can be broadened by the existence of stacking faults and the possibility of a "partial relaxation" of the K atoms, as discussed below. This gives rise to significant intensity being observed for  $l=0$ , as shown, for example, in Fig. 13(a) for the main  $(10.l)_K$  reflection. For practical reasons we shall compare the intensities observed and calculated at  $l=0$  for all six reflections considered here.

The results are presented in Table I and Fig. 21. The intensities have been normalized with respect to the strongest reflection, the  $(10.0)_M$  satellite (labeled  $b$ ) which is in plane. The stacking faults are not considered in the calculations and their influence will be assessed later. If the K atoms are shifted all the way to the center of the nearest hexagon, or in other words, if they are fully relaxed or registered, then one observes an evident failure of the model in that the out-of-plane reflections give a negligible intensity contribution for  $l=0$ , which is of course expected. We have attempted to slightly modify the model by assuming that the K atoms are not fully relaxed in the hexagon centers, as a result of a compromise between the K-K and K-graphite interactions. A simple way to account for this possible situation is to shift the K atoms until they reach a position where they are separated from the hexagon center by a given distance  $R_0$  (the atoms which are already within a circle of radius  $R_0$  being unaffected). The influence of such a partial relaxation

can be evaluated in Table I, where calculations are presented for different values of  $R_0$ . It is seen that the intensities, in particular those of the out-of-plane reflections, are very sensitive to  $R_0$ . The best fits appear to be obtained for  $R_0$  on the order of  $0.035 \text{ \AA}$ , and Fig. 21 shows a plot of the observed intensities together with the corresponding calculated ones. The overall agreement is acceptable, and it clearly appears to be more satisfactory than that obtained by Suzuki<sup>26</sup> using the discommensuration-domain model. Moreover, the agreement in Fig. 21 could probably be improved by introducing stacking faults. These faults broaden out-of-plane reflections such as  $a$ ,  $d$ , and  $e$  and increase the corresponding calculated values for  $l=0$ , which is favorable because they appear to be too low in Table I and Fig. 21. However, introducing the stacking faults in the calculation would actually lead one to fit systematically, not only the intensity for a given  $l$  value, but its profile along  $c^*$ , or  $I(l)$ , for the main and satellite reflections. This is beyond the scope of the present semiquantitative analysis, but we show in Fig. 22 an example of such a fit for the  $(10.l)_K$  profile. The observed intensity values were taken at  $T=112.5 \text{ K}$  and were already shown in Fig. 13(a). The calculated profile was obtained using a three-layer model built from  $50a_G \times 50a_G$  losanges and  $R_0=0.02 \text{ \AA}$  for the relaxation. The stacking faults were taken into account with a formalism similar to that of Sec. III B, for the graphite stacking, and two parameters were varied: the probability  $\eta$  of faults in the  $\alpha\beta\gamma$  sequence (such as  $\alpha\beta\alpha$ , for instance) and the probability  $p$  of arbitrary translations between K layers. The calculated curve in Fig. 22 is based on best-fit parameters,

$$\eta=0.25, \quad p=0.20.$$

It turns out that these values amount exactly to those obtained in Sec. III B for the stacking disorder of the graph-

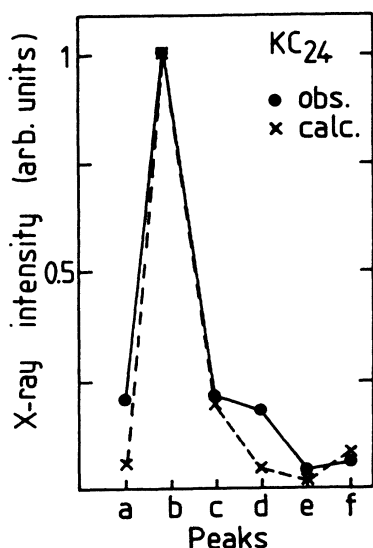


FIG. 21. Comparison of observed and calculated intensities in  $\text{KC}_{24}$  for the intermediate phase. In the calculation a partial relaxation (with  $R_0=0.035 \text{ \AA}$ ) was used. No stacking faults were introduced. The reflections are labeled  $a-f$  as in Table I and they are indicated in Fig. 11(a).

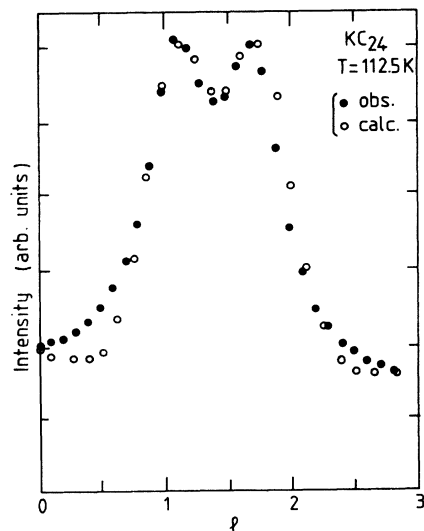


FIG. 22. Observed and calculated scans along  $l$  for the main K reflection at  $T=112.5 \text{ K}$ . A satisfactory agreement is obtained introducing both partial relaxation of the K atoms and stacking faults.

ite host. While the  $\alpha\beta\gamma$  (K) and  $ABC$  (graphite) stackings are distinct, as noted previously, it appears that the stacking disorder of the graphite host is reflected in that of the K intercalate. This occurs probably through the modulation effect of the graphite potential, i.e., through the relaxation described here.

Finally, we have tried to use the same type of model for the low-temperature structure below  $T_L$ . First it is straightforward to extend this model to the case of the oblique unit cell determined in Sec. VB using an oblique primitive lattice of K atoms as an initial structure instead of an hexagonal one. After relaxation (full or partial) one obtains a model of a layer where the distribution of K atoms is modulated by the graphite host while being, on the average, the initial oblique structure.

The next step is to stack the K layers in order to account for the observed selection rules as reported in Sec. VB. Unfortunately, these selection rules do not appear to be consistent with a unique stacking sequence. We have calculated the intensity profiles along  $l$  for several types of stacking and we have found that the best results are obtained with the stacking sequence

$$A\alpha AB\beta BC\alpha' C A\beta' AB\alpha'' BC\beta'' C$$

and a lateral shift between  $\alpha$  and  $\beta$  equal to  $\frac{1}{2}a_L + \frac{1}{2}b_L$ . This induces the proper selection rule for the following reflections: 1,2,3,6 (main) and 8,10,12,14,15 (satellites), but the failure to account for the others indicates that this question is left open.

## VII. FINAL REMARKS

We have presented a global description of the structural properties of  $KC_{24}$  and  $RbC_{24}$  single crystals from quantitative data collected from both the liquid and low-temperature-solid phases. The results reveal a similar behavior but also significant differences for these two

alkali-metal GIC's.

In the liquid state both compounds show a slight hexagonal distortion of the diffuse scattering halos (it is more pronounced for  $KC_{24}$ ). In the case of  $RbC_{24}$ , it is noted that most semiquantitative features of the intensity modulation are very nicely reproduced in the molecular-dynamics simulation of Fan *et al.*<sup>14</sup> The present data should allow a more quantitative comparison with this simulation and also, in the case of  $KC_{24}$ , with a much awaited similar molecular-dynamics study now possible using the newly determined modulation potential for  $KC_{24}$ .<sup>35</sup>

From our model calculations it is believed that the order of the K atoms in the solid phase is better described by a simple relaxed incommensurate structure similar to Diczko's<sup>29</sup> than by the discommensuration-domain model of Suzuki.<sup>26</sup> However, a more profound understanding of the differences between the two models would require more comprehensive and accurate intensity data. The question is still open all the more so since the interpretation of the quasielastic-neutron-scattering data for the liquid state, by Zabel, Magerl, and co-workers,<sup>17</sup> is based on the existence of  $\sqrt{7} \times \sqrt{7}$  domains, much above the melting temperature, with diffusive atomic motions predominantly located in or near the domain walls.

Finally, it also appears that the distinct low-temperature behavior of  $KC_{24}$  and  $RbC_{24}$  with the hexagonal-oblique transition in  $KC_{24}$  and the loss of interlayer correlations in  $RbC_{24}$ , are interesting manifestations of competing interactions and probably frustration which remain potentially attractive for future studies.

## ACKNOWLEDGMENTS

We wish to thank S. C. Moss for several stimulating and useful discussions and M. Lelaurain for her help on sample preparation and characterization.

\*Present address: Laboratoire de Microstructure et Microélectronique, CNRS, 196 avenue Henri Ravera, 92220 Bagneux, France.

<sup>1</sup>S. A. Solin, *Adv. Chem. Phys.* **49**, 455 (1982).

<sup>2</sup>M. S. Dresselhaus and G. Dresselhaus, *Adv. Phys.* **30**, 139 (1981).

<sup>3</sup>R. Clarke and C. Uher, *Adv. Phys.* **33**, 469 (1984).

<sup>4</sup>H. Zabel and P. C. Chow, *Comments Solid State Phys.* **12**, 225 (1986).

<sup>5</sup>R. Moret, in *Intercalation in Layered Materials*, Vol. 148 of *NATO Advanced Study Institute Series B: Physics*, edited by M. S. Dresselhaus (Plenum, New York, 1986), p. 185.

<sup>6</sup>S. C. Moss and R. Moret, in *Graphite Intercalation Compounds: Structure and Dynamics*, Vol. 1 of *Springer Series on Topics in Current Physics*, edited by H. Zabel and S. A. Solin (Springer, New York, 1990).

<sup>7</sup>F. Rousseaux, R. Moret, D. Guerard, P. Lagrange, and M. Lelaurain, *J. Phys. (Paris) Lett.* **45**, 1111 (1984).

<sup>8</sup>F. Rousseaux, R. Moret, D. Guerard, P. Lagrange, and M. Lelaurain, *Synth. Met.* **12**, 45 (1985).

<sup>9</sup>F. Rousseaux, R. Moret, D. Guerard, P. Lagrange, and M.

Lelaurain, *Ann. Phys. (Paris) Colloq.* **11**, 85 (1986).

<sup>10</sup>D. E. Nixon and G. S. Parry, *J. Phys. C* **2**, 1732 (1969).

<sup>11</sup>G. S. Parry, *Mater. Sci. Eng.* **31**, 99 (1977).

<sup>12</sup>G. Reiter and S. C. Moss, *Phys. Rev. B* **33**, 7209 (1986).

<sup>13</sup>S. C. Moss, G. Reiter, J. L. Robertson, C. Thompson, J. D. Fan, and K. Ohshima, *Phys. Rev. Lett.* **57**, 3191 (1986).

<sup>14</sup>J. D. Fan, O. A. Karim, G. Reiter, and S. C. Moss, *Phys. Rev. B* **39**, 6111 (1989).

<sup>15</sup>S. C. Moss, X. B. Kan, J. D. Fan, J. L. Robertson, G. Reiter, and O. A. Karim, in *Competing Interactions and Microstructure: Statics and Dynamics*, edited by R. Lesar, A. Bishop, and R. Heffner (Springer-Verlag, New York, 1988), p. 158.

<sup>16</sup>W. A. Kamitakahara and H. Zabel, *Phys. Rev. B* **32**, 7817 (1985).

<sup>17</sup>The quasielastic-neutron-scattering work is reviewed in H. Zabel, A. Magerl, J. J. Rush, and M. E. Misenheimer, *Phys. Rev. B* **40**, 7616 (1989).

<sup>18</sup>G. S. Parry and D. E. Nixon, *Nature* **216**, 909 (1967); G. S. Parry, D. E. Nixon, K. M. Lester, and B. C. Levene, *J. Phys. C* **2**, 2156 (1969).

<sup>19</sup>R. Clarke, N. Caswell, S. A. Solin, and P. M. Horn, *Phys.*

- Rev. Lett. **43**, 2018 (1979).
- <sup>20</sup>R. Clarke, J. N. Gray, H. Homma, and M. J. Winokur, Phys. Rev. Lett. **47**, 1407 (1981).
- <sup>21</sup>J. B. Hastings, W. B. Ellenson, and J. E. Fischer, Phys. Rev. Lett. **42**, 1552 (1979).
- <sup>22</sup>H. Zabel, S. C. Moss, N. Caswell, and S. A. Solin, Phys. Rev. Lett. **43**, 2022 (1979).
- <sup>23</sup>R. Clarke, N. Caswell, and S. A. Solin, Phys. Rev. Lett. **42**, 61 (1979).
- <sup>24</sup>Y. Yamada and I. Naiki, J. Phys. Soc. Jpn. **51**, 2174 (1982).
- <sup>25</sup>M. Suzuki and H. Suematsu, J. Phys. Soc. Jpn. **52**, 2761 (1983).
- <sup>26</sup>M. Suzuki, Phys. Rev. B **33**, 1386 (1986).
- <sup>27</sup>M. Mori, S. C. Moss, Y. M. Jan, and H. Zabel, Phys. Rev. B **25**, 1287 (1982).
- <sup>28</sup>M. J. Winokur and R. Clarke, Phys. Rev. Lett. **54**, 811 (1985).
- <sup>29</sup>S. B. DiCenzo, Phys. Rev. B **26**, 5878 (1982).
- <sup>30</sup>M. J. Winokur and R. Clarke, Phys. Rev. B **34**, 4948 (1986).
- <sup>31</sup>M. Suzuki, H. Ikeda, H. Suematsu, Y. Endoh, and H. Shiba, Physica **105B**, 280 (1981).
- <sup>32</sup>V. B. Cajipe and J. E. Fischer, Phys. Rev. B **35**, 4854 (1987).
- <sup>33</sup>F. Rousseaux, D. Tchoubar, C. Tchoubar, D. Guerard, P. Lagrange, A. Herold, and R. Moret, Synth. Met. **7**, 221 (1983).
- <sup>34</sup>K. Ohshima, S. C. Moss, and R. Clarke, Synth. Met. **12**, 125 (1985).
- <sup>35</sup>X. B. Kan, J. L. Robertson, S. C. Moss, K. Ohshima, and C. J. Sparks, Phys. Rev. B **39**, 10 627 (1989).
- <sup>36</sup>H. Mitani and H. Morita, Synth. Met. **12**, 335 (1985).
- <sup>37</sup>M. Suzuki, H. Ikeda, H. Suematsu, Y. Endoh, H. Shiba, and M. T. Hutchings, J. Phys. Soc. Jpn. **49**, 671 (1980).
- <sup>38</sup>D. G. Onn, G. M. T. Foley, and J. E. Fischer, Phys. Rev. B **19**, 6474 (1979).
- <sup>39</sup>H. Suematsu, M. Suzuki, and H. Ikeda, J. Phys. Soc. Jpn. **49**, 835 (1980).
- <sup>40</sup>Aberkane, F. Rousseaux, E. J. Samuelsen, and R. Moret, Ann. Phys. (Paris) Colloq. **11**, 95 (1986).

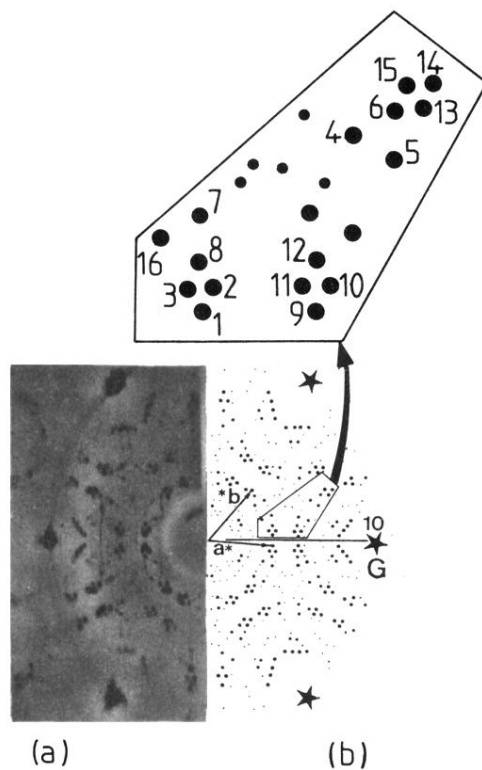


FIG. 16. Left (a) is a portion of a monochromatic Laue photograph from a  $KC_{24}$  single crystal in the low-temperature phase.  $Cu K\alpha$  x-ray radiation and a cylindrical camera have been used. Right (b) gives a drawing of the reciprocal lattice obtained with a unique oblique 2D lattice (plus the symmetry-induced twins). The comparison between the observed and simulated patterns is satisfactory. The inset shows an enlarged portion of the simulated pattern where selected r.l. peaks are numbered.